

# NASA Technical Paper 1449

LOAN COPY: RETURN TO  
AFWL TECHNICAL LIBRARY  
KIRTLAND AFB, NM



## Analytical Prediction With Multi-dimensional Computer Programs and Experimental Verification of the Performance, at a Variety of Operating Conditions, of Two Traveling Wave Tubes With Depressed Collectors

James A. Dayton, Jr., Henry G. Kosmahl,  
Peter Ramins, and Norbert Stankiewicz

MAY 1979





NASA Technical Paper 1449

Analytical Prediction With Multi-dimensional Computer Programs and Experimental Verification of the Performance, at a Variety of Operating Conditions, of Two Traveling Wave Tubes With Depressed Collectors

James A. Dayton, Jr., Henry G. Kosmahl,  
Peter Ramins, and Norbert Stankiewicz  
*Lewis Research Center*  
*Cleveland, Ohio*

**NASA**

National Aeronautics  
and Space Administration

**Scientific and Technical  
Information Office**

1979

## SUMMARY

Experimental and analytical results are compared for two high performance, octave bandwidth, traveling wave tubes (TWT's) that used multistage depressed collectors (MDC's) to improve the efficiency. The computations were carried out with advanced, multidimensional computer programs that are described here in detail. These programs model the electron beam as a series of either disks or rings of charge and follow their multidimensional trajectories from the radiofrequency (rf) input of the ideal TWT, through the slow wave structure, through the magnetic refocusing system, to their points of impact in the depressed collector. Traveling wave tube performance, collector efficiency, and collector current distribution were computed and the results compared with measurements for a number of TWT-MDC systems. Power conservation and correct accounting of TWT and collector losses were observed.

For TWT's operating at saturation, very good agreement was obtained between the computed and measured collector efficiencies. For a TWT operating 3 and 6 decibels below saturation, excellent agreement in computed and measured collector efficiencies was obtained in some cases but only fair agreement in others. However, deviations can largely be explained by small (<5 percent) differences in the computed and actual spent beam energy distributions.

The analytical tools used here appear to be sufficiently refined to design efficient collectors for this class of TWT. However, for maximum efficiency, some experimental optimization (e.g., collector voltages and aperture sizes) will most likely be required.

## INTRODUCTION

The operation of future space and airborne high power transmitting systems in the microwave frequency range has imposed difficult efficiency and other performance requirements on traveling wave tubes (TWT's). For improved efficiency, TWT's will almost always be designed and operated with multistage depressed collectors (MDC's) (refs. 1 to 3). The design of highly efficient collectors and (to a lesser degree) efficient TWT's requires, in turn, the availability of an accurate, multidimensional, large signal computer program whose output describes not only the radiofrequency (rf) performance of the TWT but also the velocity vectors and radii of the electrons that enter

the depressed collector. This method reduces significantly the number of costly, time consuming iterations, or cut and try approaches, and may eventually offer an accurate "a priori" computational design procedure. For this purpose, the Lewis Research Center is carrying out an extensive analytical, computational, and experimental program to improve the efficiency of TWT's for use in space and, jointly with the U.S. Air Force, of TWT's for use in airborne electronic countermeasure systems by applying designs, programs, and techniques developed at Lewis. The experimental program stresses accurate and complete TWT and MDC evaluations, verification of a strict power balance, and identification of sources and magnitudes of losses in the TWT-MDC system.

In this paper, we discuss the computer programs and physical models describing the large signal amplification and the electron flow through the TWT and the MDC and compare the analytical and experimental data in detail. To our knowledge this is the first time that actual multidimensional electron trajectories, including space charge interaction effects, have been followed from the TWT rf input to their final termination on the MDC electrodes. In mathematical complexity, this method is equivalent to describing the flow of a compressible, turbulent, viscous (space charge forces) fluid, with the additional complications of electromagnetic traveling waves and impressed static magnetic fields.

## LEWIS RESEARCH CENTER MULTIDIMENSIONAL HELICAL TWT PROGRAM

### GENERAL PROGRAM CHARACTERISTICS

A large number of publications (notably, ref. 4) have been dedicated to the treatment and modeling of TWT's. The reader is assumed to be familiar with the nomenclature and customary use of circuit, rf wave, and space charge parameters and formulations. The important parameters are defined in the symbol list (appendix B).

The helical TWT computer program, written in structured FORTRAN by C. Farrell of the Lewis Research Center, was evolved through a series of extensive modifications and additions to a program and formulation originally developed by H. Detweiler (ref. 5) who, in turn, used Rowe's circuit beam coupling formulation (ref. 4). Some of the additions were suggested by Detweiler himself and deal with deficiencies of his original formulation; these concern the introduction of

- (1) Radiofrequency circuit losses
- (2) Attenuators and severs
- (3) Changes in phase velocity and circuit impedance
- (4) Changes in circuit radius

Further, we added an accurate formulation of

- (1) Periodic permanent magnet (PPM) focusing fields
- (2) A relativistic correction to the axial equation of motion
- (3) A solution of the complete second-order circuit equation for the rf wave
- (4) The retention of terms multiplying  $C^2$  (Pierce's gain parameter  $C$ )
- (5) An optional split of the 32 deformable disks (per rf cycle) into 96 rings, which are flexible in both the axial and radial directions
- (6) The use of an actual "hot" phase velocity for the beam-loaded rf wave on the helix instead of the (constant) "cold" phase velocity
- (7) The optional inclusion of the backward wave

### CALCULATION AND COMPUTATION OF SPACE CHARGE FORCES

The performance of a TWT can be formulated by using a Lagrangian analysis for the electron beam, which is divided into 32 disks that, in turn, are each (optionally) split into three rings, for a total of 96 rings per rf cycle.

An explicit expression for the space charge fields can be obtained by solving Poisson's equation by the Green's function method. It is assumed that the helix surrounding the beam is a perfectly conducting tube and that the disks are thin in the axial direction  $z$ . The deformable disk model uses a radial integration over all space charges at a given  $z$  location. From the space charge potential expression, axial and radial space charge fields are obtained by differentiation. The resulting expressions for the radial and axial fields are

$$E_{sc-r}(r, z) = \text{Constant} \int_0^{2\pi} \sum_{n=1}^{\infty} \frac{J_1\left(\lambda_n \frac{r}{a}\right) J_0\left(\lambda_n \frac{r'}{a}\right) \exp\left(-\frac{\lambda_n}{\beta_e a} |\Phi - \Phi'|\right)}{[J_1(\lambda_n)]^2} d\Phi'_0 \quad (1)$$

$$E_{sc-z}(r, z) = \text{Constant} \int_0^{2\pi} \sum_{n=1}^{\infty} \frac{J_0\left(\lambda_n \frac{r}{a}\right) J_0\left(\lambda_n \frac{r'}{a}\right) \exp\left(-\frac{\lambda_n}{\beta_e a} |\Phi - \Phi'|\right)}{[J_1(\lambda_n)]^2} \times \text{sgn}(\Phi - \Phi') d\Phi'_0 \quad (2)$$

In these equations the primed quantities denote the source charges, and the unprimed quantities denote the reference charge for which the space charge field is sought;  $\lambda_n$  are the roots of the equation  $J_0(\lambda_n) = 0$ ;  $\beta_e a = (\omega/u)a$ ; and  $\Phi$  and  $\Phi_0$  are the phase position and entrance phase position, respectively, of the ring (disk) relative to the rf wave. Evaluating these equations would be a very time-consuming matter, even on a large computer, if the evaluations were to be carried out at each of the several thousand displacement planes  $z$  for the several radial locations of the source and the reference disk. To simplify the problem, Rowe (ref. 4) introduced a useful procedure that involves dividing the cross section of the interaction region into a number of annular (axisymmetric) regions. The weighting functions, equations (1) and (2), are calculated for specific values of  $|\Phi - \Phi'|$  at radii corresponding to the midradius of each radial region (maximum number, 10) and are then stored in the computer memory. In the execution of the rf interaction program the computer is instructed to scan the table of the space charge weighting function subroutine and to determine the appropriate space charge forces. This procedure results in certain inaccuracies.

The space charge forces calculated with equations (1) and (2) are, strictly speaking, those arising from a continuous distribution of charges, that is, infinitesimally thin disks (rings). The space charge forces between the finite thickness disks will be slightly different, with the difference being significant only when the separation between the disks becomes small and during the actual overlapping of finite thickness disks. When two identical disks overlap completely, the axial space charge force between them is exactly zero. Thus, the effect of overlapping can be taken into account by truncating the axial space charge forces linearly to zero at  $(\Phi - \Phi') = 0$  from their respective values at an axial phase (distance) separation  $|\Phi - \Phi'| = 2\pi/M$  (where  $M$  is the number of disks per rf cycle). The difference  $|\Phi - \Phi'| = 2\pi/M$  represents the initial (phase) width of the disks. The error involved in this truncation decreases with increasing  $M$ . For  $M = 32$ , as used in this program, the truncation error in the axial force is less than a few percent. To compute the space charge forces with 96 rings, we used an efficient program developed by T. O'Malley of Lewis.

## INPUTS AND PARAMETERS

The (helical) TWT can be conveniently divided into a number of sections whose boundaries and other characteristics are described by number cards and parameter cards (e.g., the local phase velocity, losses, impedance, and magnetic field). Most PPM-focused TWT's apply a magnetic field profile that is stronger at the TWT rf output than at the rf input. An easy and quite accurate way to model it is to raise the peak

value from section to section and place the discontinuity into the sever or attenuator region. Frequently, two or three magnetic field levels different from each other will suffice.

Two formulations are available to describe the PPM focusing field: either a simple cosine, or a compound cosine with four Fourier harmonics ( $m = 1, 2, 5, 7$ ). The simple cosine formulation assumes the absence of harmonics in describing the field; the compound cosine formulation requires the (measured) values of  $B_z(r = 0, z)$  on the axis over a full magnetic period. The program then calculates  $B_z(r, z)$  and  $B_r(r, z)$  with four cosine terms, satisfying the  $\text{div } \vec{B} = 0$  equation. If, for simplicity, the simple cosine formulation is chosen, better agreements with experiments are obtained if the amplitude of the fundamental cosine term is, not the value of the full peak field  $\hat{B}$  on the axis, but rather  $\hat{B}(4/\pi)\sin(\pi g/L)$  (or slightly more), where  $g$  and  $L$  denote the magnetic gap and period, respectively. (The value  $(4/\pi)\sin(\pi g/L)$  is the fundamental term in the Fourier expansion of a "square" wave magnetic field between the pole pieces.) The resulting difference in computer output occurs both in electron trajectories and in the rf performance because of changes in beam ripple and rf coupling.

Circuit losses are specified in decibels per inch individually for as many as 10 sections. In attenuators the rf voltage on the circuit and the power flow are present and change continuously. In severers (as many as 5), the rf parameters are set to zero, but the bunching and rf space charge forces are retained. The correct initial conditions on the circuit set up the rf wave at the end of the sever.

Velocity tapers are programmed by assuming the conservation of power; that is,  $|V_1|^2/Z_1 = |V_2|^2/Z_2$  at the interfaces between regions of different phase velocity, for all frequencies. Any reflections from discontinuities in actual tubes (unknown imperfections) are not treated.

## RING AND DISK MODELS

It is important to point out the differences between the 32-disk and 96-ring formulations. Although the disks are radially deformable, the axial forces on them - originating from the circuit as well as from space charges - are averaged over the radius of the disk and the average is applied. The result is that all parts of the disk move with the same axial velocity and the disk cross-section remains a rectangle. This is approximately correct in the small signal region as long as deviations from the direct current injection velocity are small. Whenever higher accuracy or more detail concerning the vector components of the spent electron beam are required, a "switch" from 32 disks to 96 rings is provided as an option. To conserve computer time, we at Lewis activated the switch at the 2 percent efficiency level. Since they change much

more slowly than the rf forces, the space charge forces were computed in the ring model every 10 to 20 axial steps of the circuit parameters (optional between 20 and 1). Radial, axial, and azimuthal forces were computed and applied at the ring centroids.

Naturally, all programs with variable size beams and rf coupling that changes with distance and radius are more difficult to execute, interpret, and use than simple one-dimensional formulations. Real benefits will result, however, only when cold tube parameters and initial beam size are known accurately. Initial beam size is critically important and should be matched to the existing magnetic field at the input. Otherwise, excessive beam rippling will result and lead to inaccurate coupling and interception. The initial beam size is also important in determining the axial injection velocity (and, therefore,  $\bar{b}$ ) because part of the beam potential energy at the cathode  $V_0$  is converted to rotational kinetic energy and space charge potential energy (depression). Errors of a few hundred volts in  $V_{\text{eff}}$  (the part of  $V_0$  that is converted to axial electron kinetic energy) can result from working with an incorrect beam size. The program computes and prints out automatically the effective potential at the helix input by using the equation

$$\frac{V_{\text{eff}}}{V_0} = 1 + \frac{b^2 \omega_L^2}{2 \frac{e}{m} V_0} \left( 2 \ln \frac{b}{a} - 1 \right) \quad (3)$$

where  $\omega_L = \omega_c/2 = eB_0/2m_0$  is the effective Larmor frequency. For  $B_0$ , the required input to the program, either a constant magnitude (solenoid) or the "effective" cosine value

$$\frac{\hat{B}4}{\pi} \sin\left(\frac{\pi g}{L}\right)$$

should be used for PPM focusing. The term in parentheses in equation (3) is negative since the ratio of beam radius to helix radius  $b/a$  is less than 1. Thus,  $V_{\text{eff}}/V_0$  is less than 1 and the amount of potential depression is given by

$$\Delta V = 1 - \frac{V_{\text{eff}}}{V_0}$$

The term  $\Delta V$  is strongly affected by errors in  $b$  and  $B_0$ . The derivation of equation (3) is given in appendix A. The axial injection velocity at the rf input is computed by using the equation



$$u_{\text{eff}} = c \left[ 1 - \frac{1}{\left( 1 + \frac{e V_{\text{eff}}}{m_0 c^2} \right)^2} \right]^{1/2} \quad (4)$$

Since most helical TWT's work with voltages of less than 10 kilovolts, relativistic corrections need not be extensive. The only important relativistic correction needed in this program concerns the axial velocity. The axial force equation

$$F_z = m \frac{du}{dt} = m \ddot{z} \quad (5)$$

was corrected by introducing the "longitudinal" mass  $m$ , where

$$m = m_0 \left( 1 - \frac{u^2}{c^2} \right)^{-3/2} \quad (6)$$

This changed equation (5) into

$$\left. \begin{aligned} F_z &= m_0 \left( 1 - \frac{u^2}{c^2} \right)^{-3/2} \frac{du}{dt} \\ \frac{du}{dt} &= \frac{F_z}{m_0} \left( 1 - \frac{\dot{z}^2}{c^2} \right)^{3/2} = \ddot{z} \end{aligned} \right\} \quad (7)$$

In equation (5) the expression for the axial force  $F_z$  was multiplied by

$$\left( 1 - \frac{\dot{z}^2}{c^2} \right)^{3/2}$$

Errors of 1 to 2 percent in energy arise from neglecting this correction at  $V_0 = 10$  kilovolts and correspond to 100 to 200 electron volts that would otherwise be lost in the power balance. Since  $\dot{r}$  and  $r\dot{\phi}$  are about a tenth of  $\dot{z}$ , there is no need to apply the correction to the transverse components. The small correction in the space charge

potential due to relativity has a negligible effect on the total performance of a TWT and is not implemented.

As would be expected, calculating tube performance with 32 deformable disks in one case and 96 rings in the other leads to somewhat different results in gain and power output. Agreement with experiments can be secured by adjusting slightly downward, in the ring case, the phase velocity parameter  $\bar{b} = (u_{\text{eff}} - v_p)/Cv_p$  and/or the normalized input power amplitude  $A_0 = \sqrt{P_{\text{in}}/2CI_0V_{\text{eff}}}$ . This process is easily understood by following the evolution of the model from Pierce's small signal theory through the deformable disk model to the ring model. In Pierce's theory, C is determined for a rigid, constant diameter beam. In the deformable disk model, C is determined for a variable size beam but is still averaged over its radius. In the ring model, each ring is weighted individually. Because of nonlinear coupling the "effective C" appears to be larger in the ring model than in the other formulations. When small signal  $\bar{b}$  is reduced (in the output section) by about 5 percent or less, the ring model produces rf results similar to those obtained with the deformable disk model. Other subtle changes in TWT parameters, notably, the input power, may alone suffice to obtain closer agreement.

Also, it must be stressed that each of the experimentally determined TWT input parameters has an associated accuracy of measurement. Therefore, each of the input parameters is actually known only within those limits of accuracy. In some cases (e.g., the input power and initial beam size) this is considerably more than a few percent.

## RESULTS OF HELICAL TWT PROGRAM

### WATKINS-JOHNSON TWT 3633-5

The accuracy of the multidimensional TWT program was verified on a Watkins-Johnson TWT for which accurate cold test data were available. This TWT - which has PPM focusing, two attenuators, one sever, and velocity tapers (all of which are included in the computation) - has the following performance characteristics:

- (1) Frequency, 2.0 to 4.0 gigahertz
- (2) Radiofrequency output power,  $\leq 576$  watts
- (3) Perveance,  $1.0 \times 10^{-6} \text{ A/V}^{3/2}$
- (4) Electronic efficiency,  $\leq 21.3$  percent

The results are summarized in table I. The agreement between the data measured by Watkins-Johnson and the computed TWT performance was very good for both the disk and ring models. This agreement was achieved by a 5 percent downward adjustment

of only the input signal amplitude  $A_0$ ; none of the other measured TWT input parameters were changed.

As already discussed, the computer models not only calculate the rf performance of the TWT, but also characterize the electron beam before, at, and beyond the rf output. As an example, the 96-ring-model spent beam characteristics at the rf output (for the 3-GHz saturated output case of table I) are shown in table II. Listed for each ring (after sorting in order of increasing kinetic energy) are the following:

- (1) The total (relativistically corrected) kinetic energy of each ring
- (2) The axial plus radial kinetic energy
- (3) The rotational (azimuthal) energy
- (4) The centroid radius
- (5) The centroid exit angle

The numbering of the rings is such that rings 1, 4, 7, 10, . . . are adjacent to the axis; rings 2, 5, 8, 11, . . . are the middle rings; and rings 3, 6, 9, 12, . . . are the outer rings of each of the 32 disks into which one rf cycle of the beam is divided axially. A closer study of the radial and axial locations of the rings relative to their small signal positions reveals that the flow is nonlaminar in both the axial and radial directions (i.e., extensive axial and radial crossovers of rings occur). This feature has three causes: the PPM focusing forces, which cause some ripple; the axial space charge forces, which are largest on the axis and zero at the helix; and the rf circuit forces on the rings. The rf circuit fields are described in terms of modified Bessel functions and, as such, increase nonlinearly with the radius. Also, rings located in the decelerating rf phase of the circuit fields are compressed toward the axis and those located in the accelerating phase experience diverging forces. The resultant motion is then a complex superposition of these effects; some "averaging" occurs, however, because of the extensive radial crossover of rings.

As expected, the azimuthal and radial energies are much smaller (typically two orders of magnitude smaller) than the axial energy. The range of angles is between  $-10^\circ$  and  $12^\circ$ , with about a quarter of the rings having negative angles. The spread in the kinetic energy of the rings is also very substantial. Although the original effective potential at the rf input is 5723 electron volts, the kinetic energies at the rf output range between 2120 and 8620 electron volts. The degree of the spread (for a given electronic efficiency) is a strong function of the beam perveance, as shown in the section PERVEANCE AND SPENT BEAM VELOCITY SPREAD. The integral kinetic energy distribution of the spent beam (i.e., the fraction of beam current  $I(E)/I_0$  with a kinetic energy greater than or equal to  $E$  as a function of  $E$ ) from table II is shown in figure 1. Also shown, for comparison, is the corresponding energy distribution for the 32-disk model (3-GHz saturated output case of table I). As expected, the ring model produces a larger energy spread than the disk model because all the forces are

averaged over the entire disk in the disk model. Computed and measured MDC performances are compared, for both the ring and disk models (spent beams of fig. 1), in the section MDC ANALYSIS RESULTS AND PERFORMANCE COMPARISON FOR WATKINS-JOHNSON TWT 3633-5.

At the rf output the beam is tightly bunched and strong space charge forces can exist between the disks or rings. The resulting energy exchange can lead to a significantly altered spent beam energy distribution that, in turn, could significantly alter an optimum MDC design. To evaluate this effect, we continued to compute electron trajectories (using the disk model) beyond the rf output in a continuation of PPM focusing but with no rf circuit forces present. The resulting change (debunching) in the spent beam energy distribution significantly altered the spent beam characteristics (fig. 2). Consequently, the optimum set of MDC voltages (and possibly the MDC geometric design) for the bunched and debunched spent beams would be different. Therefore, since any MDC must be designed for the debunched beam, it can be important to treat the debunching dynamically rather than to use the spent beam characteristics at the rf output to design an MDC for a TWT.

There is in this process a second potential source of error: injecting a "static" model of the beam into the refocusing system or into the MDC instead of a "dynamic" beam model where the disks or rings enter the refocusing system or MDC in sequence of their actual arrival time. The correct model of dynamic spent beam debunching, refocusing, and injection is currently being worked on at Lewis but is not incorporated in the present investigation.

#### TELEDYNE MEC TWT 5897C

The computer program was used with the 32-disk model and the cosine formulation of PPM focusing to analyze the performance and determine the spent beam characteristics of a Teledyne MEC TWT model 5897C. This TWT has the following performance characteristics:

- (1) Frequency, 4.8 to 9.6 gigahertz
- (2) Radiofrequency output power, 325 to 515 watts
- (3) Cathode potential relative to ground potential, -9450 volts
- (4) Total direct current beam current, 0.430 ampere
- (5) Perveance,  $0.47 \times 10^{-6} \text{ A/V}^{3/2}$
- (6) Electronic efficiency, 12 to 17 percent
- (7) Focusing, PPM

Initial computation of TWT performance with the TWT parameters supplied by the manufacturer produced poor agreement with experimental measurements. However,

some of the parameters (notably, the impedance, Pierce's relative injection velocity parameter, and the beam size at the rf input) were scaled or extrapolated rather than measured. Consequently, reasonable bounds (rather than the single values provided) were put on these parameters, and the TWT performance was evaluated for various combinations within the considered range. The parameters that were considered to be accurately known (and, therefore, used directly) were cathode voltage and current, helix diameter, locations and characteristics of the velocity tapers and severs, cathode flux, and characteristics of the PPM focusing system. The computation includes a beam drift region in a continuation of the PPM focusing past the rf output.

This parametric study (believed to be unnecessary when accurate TWT parameters are available, as discussed in the section WATKINS-JOHNSON TWT 3633-5) provided several combinations of parameters that produced very good agreement with experimental measurements (at saturated output) in terms of total rf power conversion, gain, and beam interception. The spent beam characteristics from the case which produced the best agreement with experimental measurements were used for refocusing system and MDC analysis. For the same combination of TWT parameters (except the input power), the TWT performance and spent beam characteristics at 3 and 6 decibels below saturated output were also evaluated.

The computed rf performance of the TWT at saturation is described in the section MDC ANALYSIS RESULTS AND PERFORMANCE COMPARISON FOR TELEDYNE MEC TWT WITH LEWIS REFOCUSING AND MDC's. The spent beam energy distribution at the rf output is shown in figure 3. The spent beam continues through an extension of PPM focusing ( $1\frac{1}{4}$  magnetic periods) where, with the rf forces removed, debunching and some beam expansion occur. The spent beam characteristics at the end of this drift define the input to the refocusing section. Its energy distribution after debunching is shown in figure 3. Comparing the energy distributions before and after debunching shows that, even for this beam of perveance  $0.47 \times 10^{-6}$ , the effect was sufficient to appreciably change the optimum set of MDC voltages. The effect increases with beam perveance (see, e.g., the section WATKINS-JOHNSON TWT 3633-5). Therefore, it can be important to treat the debunching dynamically rather than to use the spent beam characteristics at the rf output to design an MDC for the TWT.

Because of the relatively narrow range of energies ( $0.57 \text{ eV}_0$  to  $1.13 \text{ eV}_0$ ) and the relative absence of electrons in the energy range  $0.7 \text{ eV}_0$  to  $0.9 \text{ eV}_0$ , this spent beam is well suited for depressed collectors of few stages. However, at the end of the short drift, beam expansion is incomplete and many electrons are moving inward toward the axis (the negative angles in table III). These difficulties are remedied by the refocusing system, which is discussed in the next main section.

The spent beam energy distributions for rf output powers of 3 and 6 decibels below saturation are also shown in figure 3. In general, the range of electron velocities

narrows as the rf output power is decreased and substantially more fast electrons (e.g., with energy  $\geq 0.9 eV_0$ ) are present. Because of this effect, increasingly higher MDC efficiencies can be expected for TWT operation below saturation if a sufficiently negative MDC electrode is provided. See, for example, reference 2.

A refocusing system was added to this TWT and the combination was evaluated at and below saturation with several MDC's. The refocusing system and MDC analysis are described in the sections SPENT BEAM REFOCUSING and MDC ANALYSIS. The analytical and experimental TWT and MDC performances are compared in detail in the section MDC ANALYSIS RESULTS AND PERFORMANCE COMPARISON FOR TELE-DYNE MEC TWT 5897C WITH LEWIS REFOCUSING AND MDC's.

### PERVEANCE AND SPENT BEAM VELOCITY SPREAD

It was mentioned in the section WATKINS-JOHNSON TWT 3633-5 that, as expected, the degree of velocity spread depends strongly on beam perveance. The radial and axial space charge forces are proportional to the ratio  $I_0/V_0^{1/2}$ , but the contour of the beam edge is determined directly by the focusing magnetic fields and the beam perveance  $I_0/V_0^{3/2}$ . During the large signal interaction process these forces affect the bunching and the velocity spread in the beam in a manner related to the perveance. Figure 4 is an instructive example of the effect of beam perveance on the final energy spread. The computed distribution  $I(V)/I_0$  is plotted as a function of  $V/V_0$  for three TWT's of approximately the same efficiency ( $\eta_e \approx 11$  percent) but different microperveances, 0.05, 0.5, and 1.0. Clearly, the beam with the highest perveance also produces the largest energy velocity spread, a property that adversely affects the performance and efficiency of depressed collectors.

### SPENT BEAM REFOCUSING

As discussed in references 6 and 7, the highest efficiency is achieved when the spent beam is conditioned by a refocusing system before it is injected into the MDC. Such a refocusing system would serve as an electron beam collimator by reducing the transverse components of electron velocity and by diluting the space charge forces through controlled beam expansion.

In the Watkins-Johnson production TWT 3633-5 the spent electron beam is injected directly into a two-stage depressed collector without first being conditioned, a fact that may contribute to the relatively poor collector efficiency. A refocusing system consisting of two coils was designed for the Teledyne MEC TWT 5897C and is described here.

In the refocusing calculation, the basic assumption is made that axial bunching has been dispersed in the rf free region before the beam is injected into the refocuser as discussed in the section TELEDYNE MEC TWT 5897C. If bunching had not been dispersed, it would be necessary to solve a dynamic, time-dependent problem rather than the steady state condition that is assumed. Each disk of charge in the TWT model is replaced in the refocusing section and collector by a continuous ray (ring) of current.

In general, it is not a good idea to evaluate refocusing by merely allowing a beam expansion in which the average angle of the particles becomes zero. The arithmetic average can vanish through cancellation of large negative and large positive angles, and the beam could be quite turbulent and have a wide spectrum of violent and uncollectable angles. There are also indications that an optimum distribution is one in which the angles are small and positive. Negative injection angles can be harmful. In some cases they can be accommodated, but generally they should be avoided. For these reasons the rms value of the angles is useful as a criterion to estimate the quality of refocusing (ref. 7).

A version of the Stanford Linear Accelerator Center (SLAC) computer program developed by Herrmannsfeldt (ref. 8) was used to compute the electron trajectories through the refocuser. Figure 5 shows a typical example of the 32 particle paths through the magnetic field configuration. The TWT output contains the radius of the outer edge of each disk and the angle of motion of the disk edge relative to the beam centerline. However, the SLAC program requires as input the radius and angle of motion at the centroid of each current ray. It is therefore necessary to convert (in the disk model) both the radius and the radial velocities by

$$r_e = \sqrt{2} r_c$$

$$\left(v_r\right)_e = \sqrt{2} \left(v_r\right)_c$$

where the subscripts e and c refer to edge and centroid, respectively. For small angles, that is, for  $v_r \ll v_z$ , the angles are converted in the same way.

The magnetic fields used in the SLAC program computation are ideal coil representations (refs. 9 and 10) of measured data on the refocuser axis. These refocusing field profiles were experimentally optimized to maximize the efficiency of each MDC. Included in the measurement is the last peak of the TWT PPM stack. The coil parameters used in the computer simulation of these magnetic fields (ref. 10) were found by a matrix inversion technique. This procedure removed the trial and error associated with using ideal coils to represent fields.

Trajectory integration began where  $B_z = 0$  and proceeded through the last stage of the PPM confinement field and into the double solenoid system (of opposing polarities) which is the refocuser. Because of the ideal coil representation of the magnetic field data, a third-order (six differentiations) calculation by the axial expansion formula (e.g., ref. 11) could be used for the off-axis field components.

Table III gives the input and output angles for the three magnetic field refocusers considered in this paper. The refocuser virtually eliminated negative angles and reduced the rms angle in all but the last case.

## PERFORMANCE OF MULTISTAGE DEPRESSED COLLECTOR

### MDC ANALYSIS

The multistage depressed collector was also analyzed with the same version of the SLAC electron trajectory program developed by Herrmannsfeldt (ref. 8) that was used in analyzing the refocuser. In this application, Poisson's equation was solved for the specific electrode geometry and the potentials defined by the MDC in the presence of the electron beam. The electron trajectory equations are fully relativistic and account for the axisymmetric electric field distribution within the collector, including all space charge effects and the magnetic field that penetrates through the output polepiece aperture of the refocusing system.

The number of depressed stages is defined as the number of distinct voltages (other than ground) needed to operate the MDC. For example, a three-stage depressed collector is one which operates with three depressed voltages, although it may have more than three collecting elements or stages.

Electron trajectories were followed to their termination (collection) on the MDC electrodes, and both the dissipated power (residual kinetic energy) and the recovered power were determined. Impact energy was computed by subtracting the change in potential energy from the kinetic energy at the input to the MDC. The effects of secondary electrons could only be estimated. In this analysis it was assumed that all electron impacts on the MDC electrodes generated low energy secondary electrons (yield:  $\delta = 1/2$  for carbon black,  $\delta = 1$  for copper), with the local electric field determining whether they were suppressed or accelerated to less depressed electrodes.

This MDC analysis was performed for the precise electrode geometry and voltages of the MDC of the Watkins-Johnson TWT 3633-5 and for each of the three depressed collectors described in reference 2 and used in conjunction with the Teledyne MEC TWT 5897C. Because computation of the potential depression at the TWT input was only approximate for the non-Brillouin flow in these TWT's, because the computations of space charge depression and rotational energy by the two computer programs



differed, and because the disks or rings were injected as continuous rays of current into the refocusing section and MDC, the effective potential was defined by the requirement of an accurate final energy balance. Iterative computation was required, and a final energy balance within approximately 0.5 percent was considered acceptable. These corrections were less than 1.4 and 5.0 percent for the Teledyne MEC and Watkins-Johnson TWT's, respectively.

## MDC ANALYSIS RESULTS AND PERFORMANCE COMPARISON FOR WATKINS-JOHNSON TWT 3633-5

A production model of the Watkins-Johnson TWT 3633-5 was analyzed by the computing methods previously described, and the results were compared with data provided by Watkins-Johnson. An analysis of this tube's rf performance has already been presented. The tube was equipped with a two-stage collector but had no refocusing system. No collector efficiency data were available, only the collector current distribution. The TWT 3633-5 was analyzed by using both the 32-disk and 96-ring models.

The results of the 32-disk analysis are shown in table IV, and the trajectories in figure 6. In all the trajectory plots in this paper the lines intersecting the system axis of symmetry at right angles are equipotential lines normalized to  $V_0$ . The secondary currents were computed by assuming a secondary yield  $\delta$  of 1.0 for the copper collector surfaces. Although there was no spike plate to deflect electrons impacting the second stage from the axis, it was assumed in constructing table IV that no secondaries produced by primary electrons that passed the entrance aperture of the second stage were able to escape because of the large aspect ratio of this stage. The agreement with measured values of current was fair. The current to stage 2 was in error by three rays; the first-stage error was one ray; and the backstreaming error was two.

Much closer agreement with measured current was obtained with the 96-ring model, as shown in table V and figure 7. Here the same assumptions were made regarding secondary yield and collection. The agreement with measured values was excellent.

The analysis of the results depends on the assumption of a secondary yield of 1.0. No attempt was made to measure the secondary yield, and it is known (ref. 12) that the secondary yield of a metal surface depends on a number of variables that are not necessarily controlled in manufacturing collectors of this type.

Because of the proximity of the first depressed stage, there was some leakage of the electric field from that stage into the entrance aperture of the collector. This could not be treated directly by the TWT program and was accommodated by reducing

the kinetic energies of the current rays in the spent beam by the potential energies, derived from a solution of Laplace's equation, at their locations in the aperture. No attempt was made to compute the beam dispersion that would result from the fringing field leakage.

## MDC ANALYSIS RESULTS AND PERFORMANCE COMPARISON FOR TELEDYNE MEC TWT 5897C WITH LEWIS REFOCUSING AND MDC's

The Teledyne MEC TWT was modified by adding a basic refocusing system and (successively) several MDC designs. Within its limits of variability the refocusing system was experimentally optimized individually for each MDC design. The performances of the TWT-refocusing-MDC systems were evaluated with the TWT operating at and below saturation (ref. 2). Computed and measured performances of the TWT-refocusing-MDC systems (for the operating frequency corresponding to the maximum rf output power) are compared in detail in this section. The terms "experimental" collector and "simplified" collector refer to terminology introduced in reference 2.

### TWT Operating at Saturation

The MDC geometries, applied potentials, and electron trajectories in each of the three MDC's are shown in figures 8 to 10. Analytical and experimental MDC performances are compared in detail in tables VI to VIII. The small differences in total energy, sum of currents, and TWT performance with the three MDC's are due to slightly different (<1 percent) operating conditions in the three cases.

Figures 8 to 10 clearly show that each of the three axisymmetric MDC's provided considerable dispersion (radial deflection) for all spent beam velocity classes. Backstreaming of electrons resulted only from secondary electron emission and from the very considerable collector depression used (experimentally optimized for maximum MDC efficiency not for minimum backstreaming).

Figure 8 illustrates the potential danger of lens effects in these collectors. A number of electrons had insufficient energy to reach stage 4 and began backstreaming in the presence of a convergent lens (see  $0.85 V_0$  equipotential). For slightly different injection velocities, such a convergent lens could produce backstreaming to the TWT body or to stage 1. Such lens effects can be avoided entirely, as discussed in reference 1. In the collectors discussed herein, lens effects were exploited to maximize MDC efficiency (ref. 2). This can be most effectively done when the spent beam energy

distribution shows the relative absence of certain energy classes (e.g.,  $0.7 eV_0$  to  $0.9 eV_0$  in fig. 3).

Experimental three-stage collector. - Comparing currents to the various collector stages (table VI) shows that for stages 1 to 3 the agreement between analytical and experimental values was reasonably good. For stages 4 and 5, however, it was poor. This can be largely explained by comparing the computed spent beam energy distribution with the measured data shown in figure 3. (These data were obtained from MDC tests at different electrode voltages and do not include the residual kinetic energy dissipated upon impact with the electrodes.) It is evident that the actual TWT had considerably more fast electrons (e.g.,  $E \geq 0.95 eV_0$ ) than computed. Referring to figure 8, we see that 14 of the 32 current rays should have had sufficient energy to penetrate well past stage 5 and to be collected on stages 5 and 6, with some secondaries backstreaming to stage 4. Instead, two current rays had insufficient energy to reach stage 4 or stage 5 (at  $0.92 V_0$ ) and several others were barely able to do so. Computing electron trajectories on this collector with the voltages on stages 2 to 5 reduced by 5 percent led to markedly better agreement in computed and measured currents to the upper stages. We are dealing here with subtle differences in computed and actual energy distributions and with inaccuracies in representing the large number of electrons (each with its own radius and vector velocity) within a given current ray by the motion of the ray centroid. The computed and measured collector efficiencies showed excellent agreement, largely because of three considerations:

(1) Experimental collector performance is not highly sensitive to collector voltages unless extreme depression is used (ref. 13).

(2) The smaller amount of backstreaming produced by the analytical model of the MDC compensated for the reduced current to the upper stages.

(3) The discrepancies between computed and experimental energies were small in relation to their absolute values (<7 percent for the range shown in fig. 3).

An MDC is designed primarily for collector efficiency, which is relatively insensitive to tube operating parameters (ref. 13), rather than for the current distribution to the stages, which varies considerably with tube operating conditions. Regardless of the computed current distribution at one particular operating point, it would be necessary to design the collector to tolerate a wide range of current distributions to allow for operation under other conditions.

Experimental five-stage collector. - Comparing the current distributions in table VII shows that agreement between the analytical and experimental values was poor in most respects. The disagreement for the more depressed stages can largely be explained by the differences between the computed and actual spent beam energy distributions, as already discussed. The large amount of current actually collected on

stage 2 implies the presence of a number of slightly slower electrons than computed because the average dissipated kinetic energy is so low for this collector (760 eV/electron). Small differences in energy, injection angle, and injection radius can drastically affect the current distribution without much effect on collector efficiency. The computed and measured collector efficiencies showed excellent agreement.

Simplified three-stage collector. - Comparing the current distributions in table VIII shows that the agreement between analytical and experimental values was much better than for the experimental collectors. This is due largely to the absence of the additional stages, which makes the simplified collector less sensitive to small differences between the computed and actual spent beam energy distributions and injection angles. For example, the current distributions in the experimental three-stage collector agreed considerably better if only the sums of the currents to stages 2 and 3 and to stages 4 and 5 were considered.

The computed and measured collector efficiencies showed reasonable agreement. The somewhat low computed efficiency was due entirely to the backstreaming of the secondary electrons created at the aperture of stage 2. A slight enlargement of this aperture would mitigate this problem.

### TWT Operating Below Saturation

Three-stage collectors. - The applied potentials and electron (current ray) trajectories in the simplified three-stage collector with the TWT operating at 3 and 6 decibels below saturation in output power are shown in figures 11 and 12, respectively. Analytical and experimental performances are compared in detail in tables IX and X. The agreement between the computed and measured collector current distributions was relatively poor, particularly at 6 decibels below saturation. The computed MDC efficiencies were 5.1 and 6.9 percentage points low at 3 and 6 decibels below saturation, respectively. The low MDC efficiencies in these analytical collectors were due largely to harmful lens effects, that is, the backstreaming produced by the convergent action of the electric field on electrons stopped near the inner aperture of stage 3 (figs. 11 and 12). At 3 decibels below saturation, two current rays (27 mA) backstreamed to the TWT body; at 6 decibels below saturation, one current ray backstreamed to the TWT body and several others to stage 2.

This difference in the computed and measured MDC current distributions and efficiencies can be largely explained by relatively small differences between the computed and actual spent beam energy distributions. To demonstrate this, identical beams (for 3 and 6 decibels below saturation) were injected into the MDC with the depression on stages 2 and 3 reduced by 5 percent. The results are shown in figures 13 and 14 and

tables XI and XII. The harmful lens effects have been virtually eliminated in both cases. Comparing the experimental results of tables IX and X with the analytical results of tables XI and XII for 3 and 6 decibels below saturation shows that agreement between the measured and computed collector efficiencies and current distributions was very good.

The experimental three-stage collector discussed previously exhibited slightly stronger, harmful lens effects. The computed MDC efficiencies were 6.5 and 7.2 percentage points low for 3 and 6 decibels below saturation, respectively. Reducing the depression of stages 2 and 3 considerably improved the agreement between the computed and measured collector efficiencies and current distributions.

Experimental five-stage collector. - The applied potentials and electron trajectories in the five-stage collector with the TWT operating at 3 and 6 decibels below saturation are shown in figures 15 and 16, respectively. Analytical and experimental performances are compared in detail in tables XIII and XIV. The agreement in the computed and measured current distributions was relatively poor in both cases, particularly for the upper stages. The computed and measured MDC efficiencies, however, showed very good agreement. This was due largely to two considerations:

(1) Lens effects were significantly reduced in this collector and harmful lens effects were virtually eliminated.

(2) The five-stage collector efficiency was considerably less sensitive to the particular characteristics of the spent beam.

### Scaling to Small Size

The most interesting application of the computing scheme described in this paper is not the analysis of collector data but collector design. If a mathematical model of the spent beam exiting the slow wave structure of a tube can be accurately computed, a priori collector designs can be obtained. As an illustration of how this can be done, an analytical design was made for a 2.54-centimeter- (1.0-in.-) diameter collector that could be used to replace the three-stage design, which was 4.78 centimeters (1.88 in.) in diameter (fig. 10). The result is the collector shown in figure 17, the computed performance of which is summarized in table XV for rf saturation conditions. The computed efficiency for this design was 84.4 percent, which, if achieved, would be a modest improvement over the 80.5 percent measured and the 77.1 percent computed for the simplified three-stage collector (table VIII). This demonstrates the value of such design techniques; the collector shown in figure 17 would be smaller, more efficient and easier to build than either the simplified or experimental models.

## CONCLUDING REMARKS

Electron trajectories were followed from the radiofrequency input to the traveling wave tube to their termination on the electrodes of the multistage depressed collector for a number of TWT-MDC systems by using the 32-disk and 96-ring models. In general, the agreement between computed and measured MDC efficiencies was good. The agreement between computed and measured current distributions was also good in some cases, but it was poor in others. However, the apparently poor agreement was dramatically improved by small changes (5 percent) in the collector voltages. Further studies on more TWT samples (where accurate TWT parameters are available), further refinements of analytical tools, and more extensive use of the 96-ring model to provide more detail are required to further improve the accuracy of the computations.

The analytical tools used here appear to be sufficiently refined to design efficient collectors for this class of TWT. For maximum efficiency some experimental optimization (e.g., collector voltages and aperture sizes) will most likely be required. For TWT's of higher perveance and electronic efficiency, additional verification of the design process is needed.

Lewis Research Center,  
National Aeronautics and Space Administration,  
Cleveland, Ohio, February 20, 1979,  
506-20.

## APPENDIX A

### POTENTIAL DEPRESSION DUE TO ROTATIONAL MOTION IN BEAM

Assume an ideal electron beam of constant radius  $b$  and uniform density  $\rho_0$  that moves in the positive  $z$ -direction with a constant velocity  $\dot{z} = u_{\text{eff}}$ . The beam is focused by a uniform magnetic field with Larmor frequency

$$\dot{\varphi} = \omega_L = \frac{e}{2m} B_0 = \frac{\omega_c}{2}$$

and is surrounded by a helix thought of as a perfectly conducting tube of radius  $a$ . Since  $\partial/\partial z = \partial/\partial \varphi = 0$ , the Poisson equation inside the beam,  $r < b$ , is

$$\frac{1}{r} \frac{\partial}{\partial r} (r E_r) = \frac{\rho_0}{\epsilon_0} \quad (\text{A1})$$

and between the beam edge and the helix,  $b \leq r \leq a$ , is

$$\frac{1}{r} \frac{\partial}{\partial r} \left( r \frac{\partial V}{\partial r} \right) = 0 \quad (\text{A2})$$

Integrating equation (A1) yields

$$- \frac{\partial V}{\partial r} = E_r = \frac{\rho_0}{\epsilon_0} \frac{r}{2} + c_1 \quad c_1 = 0 \quad (\text{A3})$$

Integrating equation (A2) yields

$$r \frac{\partial V}{\partial r} = c_2 \quad V = c_2 \ln \frac{r}{a} + V_0 \quad (\text{A4})$$

where  $V_0$  is the potential of the helix relative to the cathode. In the radial direction there is an equilibrium of forces, so  $\ddot{r} = 0$ . And from the force equation we then have

$$\left. \begin{aligned} r \dot{\varphi}^2 - \frac{e}{m} E_{r-\text{sc}} - \frac{e}{m} B_0 r \dot{\varphi} &= 0 \\ r \dot{\varphi}^2 - \frac{e}{m} E_{r-\text{sc}} - 2r\omega_L^2 &= 0 \end{aligned} \right\} \quad (\text{A5})$$

or

$$\left. \begin{aligned} r\omega_L^2 &= -\frac{e}{m} E_{r-sc} = -\frac{e}{m} \frac{\rho_0}{2\epsilon_0} r \\ \rho_0 &= -\frac{m\epsilon_0}{e} 2\omega_L^2 \end{aligned} \right\} \quad (\text{A6})$$

The radial potential  $\int E_r dr$  is thus  $(m/2e)\omega_L^2 r^2$  and the total kinetic potential in the beam  $V(r)$  is

$$V(r) = \frac{m}{2e} \left( u_{\text{eff}}^2 + \omega_L^2 r^2 \right) \quad (\text{A7})$$

The electron velocity inside the beam,  $\dot{z} = u_{\text{eff}}$ , is smaller than

$$u_0 = \left( \frac{2e}{m} V_0 \right)^{1/2}$$

We can determine it from the continuity requirements on  $V$  and  $E_r = \partial V/\partial r$  at  $r = b$ :

$$V(b) = \frac{m}{2e} \left( u_{\text{eff}}^2 + \omega_L^2 b^2 \right) = c_2 \ln \frac{b}{a} + V_0 \quad (\text{A8})$$

$$\left. \frac{\partial V}{\partial r} \right|_{r=b} = \frac{m}{2e} \omega_L^2 2r \Big|_{r=b} = \frac{c_2}{r} \Big|_{r=b} \quad (\text{A9})$$

from which  $c_2 = (m/2e)\omega_L^2 2b^2$  results. Equation (A8) is now rewritten

$$\frac{m}{2e} \left( u_{\text{eff}}^2 + \omega_L^2 b^2 \right) = \frac{m}{2e} 2\omega_L^2 b^2 \ln \frac{b}{a} + V_0 \quad (\text{A10})$$

We then obtain finally, for the unknown electron velocity,

$$u_{\text{eff}}^2 = \frac{2e}{m} V_0 + b^2 \omega_L^2 \left( 2 \ln \frac{b}{a} - 1 \right) \quad (\text{A11})$$

Since  $b$  must be smaller than  $a$  the term in parentheses is negative and, therefore,  $u_{\text{eff}}^2 < (2e/m)V_0$ .

The potential "depression"  $\Delta V$  is thus

$$\Delta V = \frac{m}{2e} b^2 \omega_L^2 \left( 2 \ln \frac{b}{a} - 1 \right) \quad (\text{A12})$$



and the effective potential  $V_{\text{eff}} = V_0 - \Delta V$ . The program automatically computes  $V_{\text{eff}}$ . The importance of an accurate knowledge of  $b$  and  $a$  and of  $\omega_L$  is obvious.

The preceding derivation is rigorously valid for an ideal Brillouin flow. A very good approximation for partially confined flows can be obtained by replacing the Brillouin field  $B_0$  with the quantity

$$\frac{B}{B_0} \left( \frac{\psi - \psi_c}{\pi b^2} \right)$$

where  $\psi$ ,  $\psi_c$ , and  $B$  are the actual flux for the confined flow, the cathode flux, and the actual magnetic field at the beam entrance position, respectively.

It is well known that confined-flow beams possess less rotational energy than the corresponding "Brillouin" field-focused beams. Thus the potential is less depressed for them than it is for the Brillouin beams.

## APPENDIX B

### SYMBOLS

A	normalized circuit voltage amplitude, $A =  V_c  / (ZI_0)$
$A_0$	normalized input voltage amplitude at $z = 0$ , $\sqrt{P_{in} / (2CI_0 V_{eff})}$
a	mean radius of helix
B	magnetic field, T
$\hat{B}$	peak value of magnetic field on axis in PPM stack
b	electron beam radius
$\bar{b}$	Pierce's relative velocity parameter, $(u_{eff} - v_p) / (Cv_p)$
C	Pierce's interaction parameter at helix radius, $[Z(a)I_0 / (4V_{eff})]^{1/3}$
c	speed of light in vacuum
E	electric field
e	electric charge of electron
F	force
g	length of gap between pole pieces in PPM stack
I(E)	fraction of current (electrons) in spent electron beam with kinetic energy greater than or equal to eE
$I_0$	total direct beam current
$\frac{I_0}{V_0^{3/2}}$	perveance
$J_0, J_1$	Bessel functions of zero and first order, respectively
L	length of magnetic period in PPM stack
M	number of disks per rf cycle, $M \leq 32$
m	mass of electron
P	power
$P_{in}$	input power to TWT

$P_{\text{rf}}$	rf output power of TWT
$r, \varphi, z$	cylindrical coordinates
$\text{sgn}$	$\begin{cases} 1 & \text{for } \Phi > \Phi' \\ 0 & \text{for } \Phi = \Phi' \\ -1 & \text{for } \Phi < \Phi' \end{cases}$
$t$	time
$u$	axial electron velocity, $\dot{z}$
$u_{\text{eff}}$	axial electron injection velocity at $z = 0$ , $c \left\{ 1 - \left[ 1 / \left( 1 + \frac{e}{m} \frac{V_{\text{eff}}}{c^2} \right)^2 \right] \right\}^{1/2}$
$V$	voltage
$V_0$	cathode potential relative to ground potential
$v_p$	phase velocity of rf traveling wave, frequency dependent
$Z$	characteristic (interaction) impedance of helix
$\beta_e$	axial phase constant, $\omega/u$
$\delta$	secondary electron emission yield
$\epsilon_0$	dielectric constant of vacuum
$\eta_e$	electronic efficiency of TWT, $\left( \frac{P_{\text{rf}} + \text{Circuit losses}}{I_0 V_0} \right)$
$\Theta$	phase difference between actual rf wave and reference electron traveling at $u_{\text{eff}}$
$\lambda_n$	roots of equation $J_0(\lambda_n) = 0$
$\rho_0$	electric charge density
$\Phi$	dependent phase variable, $\beta_e z - \omega t - \Theta(z)$
$\Phi_0$	entrance phase of disk with respect to rf wave at $z = 0$ (input), $(2\pi/M) j$ , $j = 1, \dots, 32$
$\psi$	magnetic flux
$\psi_c$	magnetic flux at cathode
$\omega$	operating frequency, rad/sec

$\omega_c$  cyclotron frequency,  $(e/m)B$

$\omega_L$  Larmor frequency,  $\omega_c/2$

$\omega_p$  plasma frequency,  $\left[ eI_0 / (m\pi b^2 \epsilon_0 u_{\text{eff}}) \right]^{1/2}$

## REFERENCES

1. Kosmahl, H. G.: A Novel, Axisymmetric, Electrostatic Collector for Linear Beam Microwave Tubes. NASA TN D-6093, 1971.
2. Kosmahl, H. G.; and Ramins, P.: Small-Size 81- to 83.5-Percent-Efficient Two- and Four-Stage Depressed Collectors for Octave-Bandwidth High-Performance TWT's. IEEE Trans. Electron Devices, vol. ED-24, no. 1, Jan. 1977, pp. 36-44.
3. Kosmahl, H. G.; Sauseng, O.; and McNary, B. D.: A 240 W, 12 GHz Space Communication TWT with 56 Percent Overall and 81 Percent Collector Efficiency. IEEE Trans. Electron Devices, vol. ED-20, no. 12, Dec. 1973, p. 1169.
4. Rowe, J. E.: Non-Linear Electron-Wave Interaction Phenomena. Academic Press, 1965.
5. Detweiler, H. K.: Characteristics of Magnetically Focused Large Signal Traveling-Wave Amplifiers. Ph.D. Thesis, Rep. 01094-108, University of Michigan, 1968. (RADC-TR-68-433; AD-842733.)
6. Kosmahl, H. G.: An Electron Beam Controller. United States Patent No. 3,764,850, Oct. 1973.
7. Stankiewicz, N.: Analysis of Spent Beam Refocusing to Achieve Optimum Collector Efficiency. IEEE Trans. Electron Devices, vol. ED-24, no. 1, Jan. 1977, pp. 32-36.
8. Herrmannsfeldt, W. B.: Electron Trajectory Program. SLAC-166, Stanford Linear Accelerator Center, 1973.
9. Vaughan, J. R. M.: Representation of Axisymmetric Magnetic Fields in Computer Programs. IEEE Trans. Electron Devices, vol. ED-19, no. 2, Feb. 1972, pp. 144-151.
10. Stankiewicz, N.: A Matrix Solution for the Simulation of Magnetic Fields with Ideal Current Loops. IEEE Transactions on Electron Devices, Oct. 1979.
11. Smythe, W. R.: Static and Dynamic Electricity. Third ed. McGraw-Hill Book Co., Inc., 1968, ch. 3, p. 60.
12. Forman, R.: Secondary Electron Emission Properties of Conducting Surfaces for Use in Multistage Depressed Collectors. IEEE Transactions on Electron Devices, vol. ED-25, no. 1, Jan. 1978, pp. 69-70.
13. Ramins, P.; and Fox, T.: Efficiency Enhancement of Octave-Bandwidth TWT's by the Use of Multistage Depressed Collectors. NASA TP-1416, 1979.

TABLE I. - HELICAL TWT COMPUTER MODEL VERIFICATION  
 FOR WATKINS-JOHNSON TWT 3633-5 OPERATING  
 AT SATURATION<sup>a</sup>

Frequency, GHz	Computed	Measured	Computed	Measured
	Gain, dB		Power, W	
32-Disk model				
3.0	42.04	42.0	580	576
4.0	44.6	44.8	511	520
96-Ring model				
3.0	42.35	42.0	562	576
4.0	45.2	44.8	540	520

<sup>a</sup>Typical central processing unit execution time for a broadband TWT (at one frequency), about 40 electronic wavelengths long and with a step size  $\Delta z$  of 0.005 cm (0.002 in.), is 10 to 12 minutes on a Univac 1140 computer for both models. Most of this time is consumed in calculating rf space charge forces.

TABLE II. - SAMPLE COMPUTER OUTPUT OF SPENT BEAM CHARACTERISTICS

AT rf OUTPUT FOR 96-RING MODEL<sup>a</sup>

[ 3.0-GHz case of table I.]

ELECTRON	EK (TOTAL), eV	EK (Z+R), eV	EK (PHI), eV	R, m	ANGLE, deg
93	2.123217+03	2.122758+03	4.594023-01	2.363363-03	1.585828+00
90	2.270663+03	2.270443+03	2.196334-01	1.658588-03	9.508434+00
84	2.449938+03	2.449930+03	7.561767-03	4.691689-04	1.679874+00
92	2.476461+03	2.476088+03	3.734330-01	2.121810-03	6.153356+00
91	2.502749+03	2.502427+03	3.212272-01	1.955048-03	7.150744+00
57	2.571470+03	2.571412+03	5.800471-02	9.146442-04	1.098944+01
74	2.609528+03	2.609301+03	2.276798-01	1.667569-03	1.125003+01
28	2.787264+03	2.787215+03	4.853714-02	7.770452-04	9.601769+00
30	2.824316+03	2.824265+03	5.062421-02	8.649630-04	5.848241+00
66	2.839380+03	2.839331+03	4.916478-02	8.548262-04	-1.326751+00
69	2.853820+03	2.853799+03	2.110844-02	6.264583-04	1.674910+00
75	2.854758+03	2.854746+03	1.153691-02	5.219675-04	9.886787+00
38	2.868023+03	2.868022+03	1.746680-03	3.022340-04	-3.670523-01
77	2.889797+03	2.889766+03	3.095704-02	6.751082-04	4.286640+00
73	2.943126+03	2.943098+03	2.820417-02	6.030334-04	3.823235+00
29	3.050661+03	3.050648+03	1.259296-02	4.842465-04	3.776830+00
37	3.068440+03	3.068385+03	5.432060-02	1.951684-05	6.385530-01
47	3.068554+03	3.068541+03	1.286912-02	4.877292-04	7.520912+00
68	3.158096+03	3.158053+03	4.336413-02	7.764249-04	8.407252+00
71	3.200317+03	3.200259+03	5.803929-02	8.811555-04	1.044988+01
31	3.265562+03	3.265551+03	1.139621-02	4.057124-04	-2.832603+00
63	3.360342+03	3.360264+03	7.831147-02	1.037165-03	8.442369+00
72	3.386302+03	3.386191+03	1.110436-01	1.209314-03	1.096242+01
32	3.388444+03	3.388427+03	1.690690-02	5.356428-04	-2.153834+00
39	3.414091+03	3.414069+03	2.120019-02	6.270194-04	8.192174+00
33	3.497305+03	3.497283+03	2.270146-02	6.414675-04	5.985493-01
54	3.513224+03	3.513148+03	7.626661-02	1.025235-03	6.042991+00
25	3.604024+03	3.603973+03	5.155833-02	7.987461-04	-3.486027+00
22	3.610352+03	3.610322+03	2.982155-02	6.181107-04	-4.416712+00
41	3.665816+03	3.665797+03	1.878984-02	5.563095-04	6.656599+00
27	3.715371+03	3.715289+03	8.146903-02	1.054553-03	2.202711+00
78	3.748702+03	3.748625+03	7.716955-02	1.030128-03	7.036053+00
26	3.750684+03	3.750642+03	4.257506-02	7.698138-04	-1.787345+00
34	3.760855+03	3.760847+03	7.995220-03	3.520174-04	9.924383+00
65	3.767198+03	3.767128+03	6.986873-02	9.564642-04	8.798470+00
24	3.805340+03	3.805260+03	7.959602-02	1.043884-03	1.589066+00
46	3.823584+03	3.823367+03	2.170127-01	1.607073-03	1.567815+01
45	3.823820+03	3.823698+03	1.222072-01	1.261886-03	1.121982+01
23	3.886633+03	3.886601+03	3.241081-02	6.870025-04	-3.680022+00
35	3.901210+03	3.901194+03	1.604019-02	5.254690-04	8.699408+00
64	3.931141+03	3.931074+03	6.765920-02	9.092325-04	8.346129+00
83	3.939604+03	3.939562+03	4.208517-02	7.658602-04	3.440079+00
42	3.964801+03	3.964764+03	3.701827-02	7.641464-04	1.077727+01
49	4.001921+03	4.001910+03	1.172635-02	4.101556-04	6.707012+00
67	4.015317+03	4.015305+03	1.154587-02	4.075322-04	4.908642+00
44	4.059398+03	4.059381+03	1.696838-02	5.359639-04	6.086440+00
48	4.084694+03	4.084651+03	4.238132-02	8.048843-04	7.424448+00

<sup>a</sup>Also computed (but not shown here) is the relative arrival time (at the location of the rf output) of each of the 96 rings.

TABLE II. - Concluded.

ELECTRON	EK (TOTAL), eV	EK (Z+R), eV	EK (PHI), eV	R, m	ANGLE, deg
18	4.228305+03	4.228229+03	7.600362-02	1.022803-03	-3.719215-01
36	4.274543+03	4.274531+03	1.206855-02	5.278759-04	7.907829+00
16	4.391631+03	4.391613+03	1.803997-02	4.925717-04	-9.239636+00
40	4.412040+03	4.412015+03	2.469513-02	5.665365-04	9.788054+00
17	4.457295+03	4.457258+03	3.724919-02	7.270702-04	-7.159881+00
43	4.499051+03	4.499040+03	1.076741-02	3.958119-04	4.101915+00
76	4.543986+03	4.543967+03	1.887416-02	5.023532-04	9.198622+00
62	4.620957+03	4.620948+03	9.114490-03	4.367808-04	9.196946+00
14	4.645856+03	4.645856+03	3.350859-05	2.093549-04	-7.034414+00
15	4.652733+03	4.652728+03	5.490535-03	4.368044-04	-6.161697+00
13	4.666883+03	4.666828+03	5.489595-02	8.217570-04	-1.778767+00
55	4.737800+03	4.737800+03	1.926590-04	1.049149-04	3.786853+00
89	4.779419+03	4.779157+03	2.620579-01	1.779595-03	1.160001+01
19	4.858982+03	4.858912+03	6.942164-02	9.193618-04	1.175472+00
20	4.876219+03	4.876168+03	5.121455-02	8.323355-04	-6.620694+00
21	4.888562+03	4.888473+03	8.874557-02	1.092926-03	-1.362713+00
81	4.903055+03	4.903045+03	1.010008-02	5.029943-04	5.561009+00
58	5.046262+03	5.046248+03	1.367950-02	4.368835-04	5.705677+00
53	5.220528+03	5.220447+03	8.088391-02	1.020108-03	9.588469+00
60	5.258648+03	5.258609+03	3.816387-02	7.719585-04	1.214363+01
82	5.266371+03	5.266357+03	1.322200-02	4.305467-04	1.360142+00
56	5.296233+03	5.296233+03	2.062773-05	2.114107-04	7.097555+00
51	5.334612+03	5.334579+03	3.325527-02	7.329425-04	1.047994+01
50	5.347862+03	5.347850+03	1.254599-02	4.825876-04	7.438563+00
94	5.501803+03	5.501799+03	4.467571-03	2.847619-04	6.282015+00
59	5.593183+03	5.593179+03	3.736000-03	1.381873-04	2.313177+00
4	5.630220+03	5.630154+03	6.611634-02	8.970770-04	-3.981128+00
87	5.638034+03	5.638021+03	1.281264-02	5.361908-04	7.936693+00
5	5.822174+03	5.822122+03	5.131901-02	8.320806-04	-5.483599+00
52	5.897368+03	5.897366+03	2.073559-03	2.263166-04	-4.614035-01
7	5.900326+03	5.900211+03	1.145407-01	1.170488-03	7.331533+00
6	5.997180+03	5.997072+03	1.077551-01	1.189126-03	-8.754265-01
1	6.232193+03	6.232172+03	2.064663-02	5.215754-04	9.118006+00
8	6.312297+03	6.312273+03	2.439224-02	6.119316-04	-5.923438+00
95	6.559638+03	6.559638+03	1.419382-05	2.127037-04	-7.198997-01
10	6.565181+03	6.565170+03	1.046633-02	3.903289-04	-4.267202+00
85	6.574482+03	6.574477+03	4.557679-03	2.863804-04	1.945201+00
9	6.614560+03	6.614499+03	6.147276-02	9.323707-04	5.985031+00
80	6.695091+03	6.695035+03	5.619654-02	8.648412-04	1.059458+01
11	6.777849+03	6.777811+03	3.709926-02	7.238222-04	-1.363571+00
61	7.021180+03	7.021178+03	1.958545-03	7.178040-05	-3.106073+00
86	7.112277+03	7.112177+03	9.989429-02	1.117099-03	1.147596+01
96	7.160193+03	7.160132+03	6.139626-02	9.312786-04	4.130677+00
79	7.703371+03	7.703365+03	6.578840-03	3.256368-04	6.323165+00
2	7.766497+03	7.766463+03	3.395502-02	6.969966-04	2.635463+00
12	7.881465+03	7.881381+03	8.387304-02	1.062362-03	3.909553+00
88	7.890575+03	7.890556+03	1.910970-02	5.029568-04	6.888720+00
70	8.113810+03	8.113804+03	6.059030-03	3.158523-04	4.663779+00
3	8.624975+03	8.624958+03	1.636780-02	5.747257-04	8.712403-01



TABLE III. - INPUT AND OUTPUT ANGLES OF REFOCUSING  
SYSTEMS OF TELEDYNE MEC TWT 5897C

Trajectory	Input angles, <sup>a</sup> deg	Output angles, <sup>a</sup> deg		
		Experimental two stage	Experimental four stage	Simplified two stage
1	0.18	1.95	2.37	2.3
2	2.24	1.38	1.44	1.95
3	-2.06	2.35	2.35	2.7
4	-.68	.29	.29	.35
5	.23	1.15	1.27	1.32
6	-.45	-.17	-.11	-.11
7	-1.6	2.24	2.3	2.93
8	-2.52	2.87	2.87	3.27
9	1.55	1.67	1.72	2.01
10	-2.29	2.07	2.07	2.41
11	1.55	1.84	1.9	2.18
12	1.15	1.78	1.84	2.81
13	-.68	.64	.64	.69
14	-.45	1.21	1.27	1.38
15	-2.06	2.76	2.76	3.39
16	2.58	1.55	1.61	1.9
17	2.81	1.49	1.55	1.9
18	.58	.86	.92	.98
19	.52	.98	1.15	1.15
20	4.13	.35	.41	.52
21	1.72	1.49	1.55	2.24
22	3.56	.46	.58	1.21
23	1.15	1.9	2.81	2.64
24	.98	1.67	1.72	2.18
25	-.22	1.49	1.49	1.72
26	.46	1.9	1.95	2.64
27	-1.08	.75	.81	1.04
28	1.84	1.15	1.15	1.55
29	-.17	1.27	1.27	1.38
30	-.17	2.18	2.24	2.81
31	.18	.06	.12	.12
32	-2.97	1.9	2.07	2.53
Average	0.31	1.42	1.47	1.78
rms	1.76	1.60	1.64	1.99

<sup>a</sup>For centroid of charge.

TABLE IV. - ANALYTICAL AND EXPERIMENTAL PERFORMANCES OF  
WATKINS-JOHNSON TWT 3633-5 (32-DISK MODEL)

[Computed trajectories shown in fig. 6.]

(a) MDC performance

Collecting element	Voltage, kV	Analytical			Experimental current, mA
		Current, mA	Recovered power, W	Kinetic power dissipated, W	
TWT body (interception)	0	0	0	0	0
TWT body (backstreaming)	0	0	0	0	30
Stage 1	1.95	328.1	639.8	658.7	345
Stage 2	4.65	171.9	799.3	350.1	125
Collector efficiency, percent		58.8			---

(b) Final power balance (analytical)

Total rf power conversion (includes circuit and sever losses), W . . . . .	683.7
Backstreaming to TWT body, W . . . . .	0
MDC dissipation, W . . . . .	1008.8
Recovered power, W . . . . .	1438.8
Total power, W . . . . .	3131.3
Direct current power, $I_0 V_0$ , W . . . . .	3150.0

TABLE V. - ANALYTICAL AND EXPERIMENTAL PERFORMANCES OF  
WATKINS-JOHNSON TWT 3633-5 (96-RING MODEL)

[Computed trajectories shown in fig. 7.]

(a) MDC performance

Collecting element	Voltage, kV	Analytical			Experimental current, mA
		Current, mA	Recovered power, W	Kinetic power dissipated, W	
TWT body (interception)	0	0	0	0	0
TWT body (backstreaming)	0	15.6	0	70.1	30
Stage 1	1.95	359.4	700.8	760.2	345
Stage 2	4.65	125.0	581.3	383.8	125
Collector efficiency, percent		51.4			---

(b) Final power balance (analytical)

Total rf power conversion (includes circuit sever losses), W . . . . .	647.0
Backstreaming to TWT body, W . . . . .	70.1
MDC dissipation, W . . . . .	1143.8
Recovered power, W . . . . .	1282.1
Total power, W . . . . .	3143.0
Direct current power, $I_0 V_0$ , W . . . . .	3150.0

TABLE VI. - ANALYTICAL AND EXPERIMENTAL PERFORMANCES OF TELEDYNE

MEC TWT 5897C WITH EXPERIMENTAL THREE-STAGE DEPRESSED

COLLECTOR AND TWT AT SATURATION

[Computed trajectories shown in fig. 8.]

(a) MDC performance

Collecting element	Voltage, kV	Analytical			Experimental		
		Current, mA	Recovered power, W	Kinetic power dissipated, W	Current, mA	Recovered power, W	Kinetic power dissipated, W
TWT body (interception)	0	6.4	0	44.4	3.8	0	26
TWT body (backstreaming)	0	0	0	0	13.7	0	95
Stage 1 (backstreaming)	0	13.4	0	74.5	13.5	0	87
Stage 2	5.230	73.9	386.5	188.3	72.8	380.7	63
Stage 3		174.7	913.6	227.7			
Stage 4	8.690	53.8	467.1	17.7	13.4	116.4	30
Stage 5		100.8	875.8	83.8			
Stage 6	9.440	6.7	63.4	16.3	13.5	127.4	48
Collector efficiency, percent		81.6			81.9		

(b) Final power balance

	Analytical	Experimental
Total rf power conversion (includes circuit and sever losses), W	686.9	<sup>a</sup> 690
Beam interception losses, W	44.4	<sup>a</sup> 26
Backstreaming to TWT body, W	0.0	95
MDC dissipation (includes backstreaming to stage 1), W	608.3	509
Recovered power, W	2706.4	2734
Total power, W	4046.0	4054
Direct current power, $I_0 V_0$ , W	4059.2	4054

<sup>a</sup>Using the computed value for the average energy of the intercepted electrons.

TABLE VII. - ANALYTICAL AND EXPERIMENTAL PERFORMANCES OF TELEDYNE  
 MEC TWT 5897C WITH EXPERIMENTAL FIVE-STAGE DEPRESSED COLLECTOR  
 AND TWT OPERATING AT SATURATION

[Computed trajectories shown in fig. 9.]

(a) MDC performance

Collecting element	Voltage, kV	Analytical			Experimental		
		Current, mA	Recovered power, W	Kinetic power dissipated, W	Current, mA	Recovered power, W	Kinetic power dissipated, W
TWT body (interception)	0	6.4	0	44.4	3.8	0	26
TWT body (backstreaming)	0	0	0	0	9.8	0	50
Stage 1 (backstreaming)	0	13.4	0	74.5	9.0	0	61
Stage 2	5.082	20.2	102.4	3.9	111.1	564.4	84
Stage 3	5.275	174.7	921.5	233.3	93.4	492.7	121
Stage 4	8.015	147.8	1184.7	122.4	46.0	368.4	51
Stage 5	8.838	47.0	415.7	29.9	140.0	1237.7	95
Stage 6	9.44	20.2	190.3	35.5	17.5	164.6	57
Collector efficiency, percent			84.9			84.2	

(b) Final power balance

	Analytical	Experimental
Total rf power conversion (includes circuit and sever losses), W	686.9	<sup>a</sup> 688
Beam interception losses, W	44.4	<sup>a</sup> 26
Backstreaming to TWT body, W	0.0	50
MDC dissipation (includes backstreaming to stage 1), W	499.5	469
Recovered power, W	2814.6	2828
Total power, W	4045.4	4061
Direct current power, $I_0 V_0$ , W	4059.2	4061

<sup>a</sup>Using the computed value for the average energy of the intercepted electrons.

TABLE VIII. - ANALYTICAL AND EXPERIMENTAL PERFORMANCES OF TELEDYNE

MEC TWT 5897C WITH SIMPLIFIED THREE-STAGE DEPRESSED COLLECTOR

AND TWT OPERATING AT SATURATION

[Computed trajectories shown in fig. 10.]

(a) MDC performance

Collecting element	Voltage, kV	Analytical			Experimental		
		Current, mA	Recovered power, W	Kinetic power dissipated, W	Current, mA	Recovered power, W	Kinetic power dissipated, W
TWT body (interception)	0	6.4	0	44.4	3.8	0	26
TWT body (backstreaming)	0	0	0	0	7.5	0	57
Stage 1 (backstreaming)	0	39.0	0	205.0	24.0	0	146
Stage 2	5.111	223.1	1140.1	446.1	208.3	1064.5	218
Stage 3	8.642	134.4	1161.3	69.4	168.8	1458.4	176
Stage 4	9.45	26.9	254.0	39.8	20.5	196.8	62
Collector efficiency, percent		77.1			80.5		

(b) Final power balance

	Analytical	Experimental
Total rf power conversion (includes circuit and sever losses), W	686.9	<sup>a</sup> 694
Beam interception losses, W	44.4	<sup>a</sup> 26
Backstreaming to TWT body, W	0.0	57
MDC dissipation (includes backstreaming to stage 1), W	760.3	602
Recovered power, W	2555.4	2720
Total power, W	4047.0	4099
Direct current power, $I_0 V_0$ , W	4059.2	4099

<sup>a</sup>Using the computed value for the average energy of the intercepted electrons.

TABLE IX. - ANALYTICAL AND EXPERIMENTAL PERFORMANCES OF TELEDYNE  
 MEC TWT 5897C WITH SIMPLIFIED THREE-STAGE DEPRESSED COLLECTOR  
 AND TWT OPERATING AT 3 DECIBELS BELOW SATURATION

[Computed trajectories shown in fig. 11.]

(a) MDC performance

Collecting element	Voltage, kV	Analytical			Experimental		
		Current, mA	Recovered power, W	Kinetic power dissipated, W	Current, mA	Recovered power, W	Kinetic power dissipated, W
TWT body (interception)	0	0	0	0	3.3	0	29
TWT body (backstreaming)	0	26.9	0	231.3	8.4	0	62
Stage 1 (backstreaming)	0	6.7	0	34.3	16.5	0	103
Stage 2	5.096	147.8	753.2	359.3	112.8	574.9	182
Stage 3	8.627	221.7	1912.6	148.7	283.4	2444.7	240
Stage 4	9.45	26.9	254.2	43.9	9.7	93.6	59
Collector efficiency, percent			78.1			83.2	

(b) Final power balance

	Analytical	Experimental
Total rf power conversion (includes circuit and sever losses), W	320.9	316
Beam interception losses, W	0.0	29
Backstreaming to TWT body, W	231.3	62
MDC dissipation (includes backstreaming to stage 1), W	586.2	583
Recovered power, W	2920.0	3113
Total power, W	4058.4	4102
Direct current power, $I_0 V_0$ , W	4059.2	4102

TABLE X. - ANALYTICAL AND EXPERIMENTAL PERFORMANCES OF TELEDYNE  
 MEC TWT 5897C WITH SIMPLIFIED THREE-STAGE DEPRESSED COLLECTOR  
 AND TWT OPERATING AT 6 DECIBELS BELOW SATURATION

[Computed trajectories shown in fig. 12.]

(a) MDC performance

Collecting element	Voltage, kV	Analytical			Experimental		
		Current, mA	Recovered power, W	Kinetic power dissipated, W	Current, mA	Recovered power, W	Kinetic power dissipated, W
TWT body (interception)	0	0	0	0	3.3	0	30
TWT body (backstreaming)	0	13.4	0	115.0	8.6	0	---
Stage 1 (backstreaming)	0	7.7	0	34.6	6.3	0	50
Stage 2	5.155	154.5	796.4	527.6	80.2	413.5	177
Stage 3	8.642	215.0	1858.0	140.7	328.9	2841.9	253
Stage 4	9.45	40.3	380.8	48.4	5.7	54.8	47
Collector efficiency, percent			77.8			84.7	

(b) Final power balance

	Analytical	Experimental
Total rf power conversion (includes circuit and sever losses), W	158.8	152
Beam interception losses, W	0.0	30
Backstreaming to TWT body, W	115.0	86
MDC dissipation (includes backstreaming to stage 1), W	751.3	527
Recovered power, W	3035.2	3310
Total power, W	4060.3	4104
Direct current power, $I_0 V_0$ , W	4059.2	4104



TABLE XI. - ANALYTICAL PERFORMANCE OF TELEDYNE  
 MEC TWT 5897C WITH LESS DEPRESSED SIMPLIFIED  
 THREE-STAGE COLLECTOR AND TWT OPERATING  
 AT 3 DECIBELS BELOW SATURATION  
 [Computed trajectories shown in fig. 13.]

(a) MDC performance

Collecting element	Voltage, kV	Current, mA	Recovered power, W	Kinetic power dissipated, W
TWT body (interception)	0	0	0	0
TWT body (backstreaming)	0	0	0	0
Stage 1 (backstreaming)	0	6.7	0	32.5
Stage 2	4.841	114.2	552.8	276.8
Stage 3	8.195	282.2	2312.6	262.9
Stage 4	9.450	26.9	254.2	43.6
Collector efficiency, percent	83.5			

(b) Final power balance

Total rf power conversion (includes circuit and sever losses), W . . . . .	320.9
Beam interception losses, W . . . . .	0.0
Backstreaming to TWT body, W . . . . .	0.0
MDC dissipation (includes backstreaming to stage 1), W . . . . .	615.8
Recovered power, W . . . . .	3119.6
Total power, W . . . . .	4056.3
Direct current power, $I_0 V_0$ , W . . . . .	4059.2

TABLE XII. - ANALYTICAL PERFORMANCE OF TELEDYNE  
 MEC TWT 5897C WITH LESS DEPRESSED SIMPLIFIED  
 THREE-STAGE COLLECTOR AND TWT OPERATING  
 AT 6 DECIBELS BELOW SATURATION  
 [Computed trajectories shown in fig. 14.]

(a) MDC performance

Collecting element	Voltage, kV	Current, mA	Recovered power, W	Kinetic power dissipated, W
TWT body (interception)	0	0	0	0
TWT body (backstreaming)	0	0	0	0
Stage 1 (back- streaming)	0	0	0	0
Stage 2	4.897	67.2	329.1	204.6
Stage 3	8.210	342.6	2812.7	333.8
Stage 4	9.45	20.2	190.9	29.3
Collector efficiency, percent	85.4			

(b) Final power balance

Total rf power conversion (includes circuit and sever losses), W . . . . .	158.8
Beam interception losses, W . . . . .	0.0
Backstreaming to TWT body, W . . . . .	0.0
MDC dissipation (includes backstreaming to stage 1), W . . . . .	567.7
Recovered power, W . . . . .	3332.7
Total power, W . . . . .	4059.2
Direct current power, $I_0 V_0$ , W . . . . .	4059.2

TABLE XIII. - ANALYTICAL AND EXPERIMENTAL PERFORMANCES OF TELEDYNE

MEC TWT 5897C WITH EXPERIMENTAL FIVE-STAGE DEPRESSED COLLECTOR

AND TWT AT 3 DECIBELS BELOW SATURATION

[Computed trajectories shown in fig. 15.]

(a) MDC performance

Collecting element	Voltage, kV	Analytical			Experimental		
		Current, mA	Recovered power, W	Kinetic power dissipated, W	Current, mA	Recovered power, W	Kinetic power dissipated, W
TWT body (interception)	0	0	0	0	3.2	0	29
TWT body (backstreaming)	0	0	0	0	9.3	0	70
Stage 1 (backstreaming)	0	0	0	0	7.4	0	52
Stage 2	5.082	20.2	102.7	5.3	37.0	187.9	39
Stage 3	5.275	100.8	531.7	223.1	71.5	377.2	102
Stage 4	8.015	174.7	1400.2	152.4	49.9	399.6	56
Stage 5	8.853	107.5	951.7	71.8	239.5	2120.7	143
Stage 6	9.440	26.9	253.9	44.4	11.7	110.4	55
Collector efficiency, percent		86.7			86.4		

(b) Final power balance

	Analytical	Experimental
Total rf power conversion (includes circuit and sever losses), W	321.2	311
Beam interception losses, W	0.0	29
Backstreaming to TWT body, W	0.0	70
MDC dissipation (includes backstreaming to stage 1), W	497.0	447
Recovered power, W	3240.2	3196
Total power, W	4058.4	4053
Direct current power, $I_0 V_0$ , W	4059.2	4053

TABLE XIV. - ANALYTICAL AND EXPERIMENTAL PERFORMANCES OF TELEDYNE  
 MEC TWT 5897C WITH EXPERIMENTAL FIVE-STAGE DEPRESSED COLLECTOR  
 AND TWT AT 6 DECIBELS BELOW SATURATION

[Computed trajectories shown in fig. 16.]

(a) MDC performance

Collecting element	Voltage, kV	Analytical			Experimental		
		Current, mA	Recovered power, W	Kinetic power dissipated, W	Current, mA	Recovered power, W	Kinetic power dissipated, W
TWT body (interception)	0	0	0	0	3.2	0	30
TWT body (backstreaming)	0	0	0	0	9.0	0	74
Stage 1 (back- streaming)	0	0	0	0	3.2	0	30
Stage 2	5.111	0	0	0	15.4	78.7	30
Stage 3	5.275	33.6	177.2	88.1	49.2	259.7	91
Stage 4	8.015	248.6	1992.5	186.0	68.6	549.8	67
Stage 5	8.869	114.2	1012.7	83.2	272.4	2415.8	157
Stage 6	9.440	33.6	317.2	43.1	7.3	68.8	50
Collector efficiency, percent			89.7			87.4	

(b) Final power balance

	Analytical	Experimental
Total rf power conversion (includes circuit and sever losses), W	158.8	150
Beam interception losses, W	0.0	30
Backstreaming to TWT body, W	0.0	74
MDC dissipation (includes backstreaming to stage 1), W	400.4	427
Recovered power, W	3499.6	3373
Total power, W	4058.8	4053
Direct current power, $I_0 V_0$ , W	4059.2	4053

TABLE XV. - ANALYTICAL PERFORMANCE OF TELEDYNE

MEC TWT 5897C WITH SCALED-DOWN THREE-STAGE

DEPRESSED COLLECTOR AND TWT

OPERATING AT SATURATION

[Computed trajectories shown in fig. 17.]

(a) MDC performance

Collecting element	Voltage, kV	Current, mA	Recovered power, W	Kinetic power dissipated, W
TWT body (interception)	0	6.4	0	44.4
TWT body (backstreaming)	0	0	0	0
Stage 1 (backstreaming)	0	6.7	0	33.5
Stage 2	4.993	201.6	1006.6	298.1
Stage 3	8.279	201.6	1669.0	158.3
Stage 4	9.44	13.4	126.5	27.4
Collector efficiency, percent	84.4			

(b) Final power balance

Total rf power conversion (includes circuit and sever losses), W . . . . .	686.9
Beam interception losses, W . . . . .	44.4
Backstreaming to TWT body, W . . . . .	0.0
MDC dissipation (includes backstreaming to stage 1), W . . . . .	517.3
Recovered power, W . . . . .	2802.1
Total power, W . . . . .	4050.7
Direct current power, $I_0 V_0$ , W . . . . .	4059.2

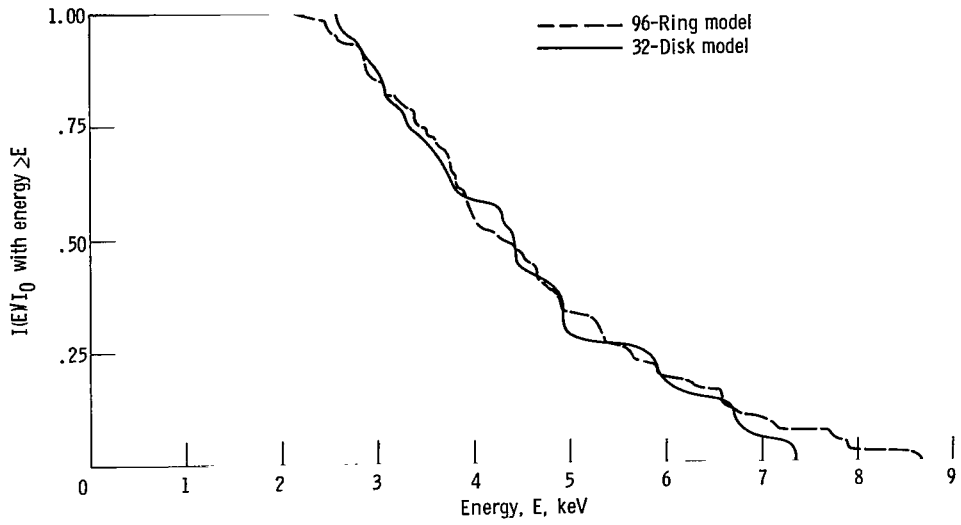


Figure 1. - Spent beam kinetic energy distribution of Watkins-Johnson TWT 3633-5 as computed with disk and ring models (at rf output).

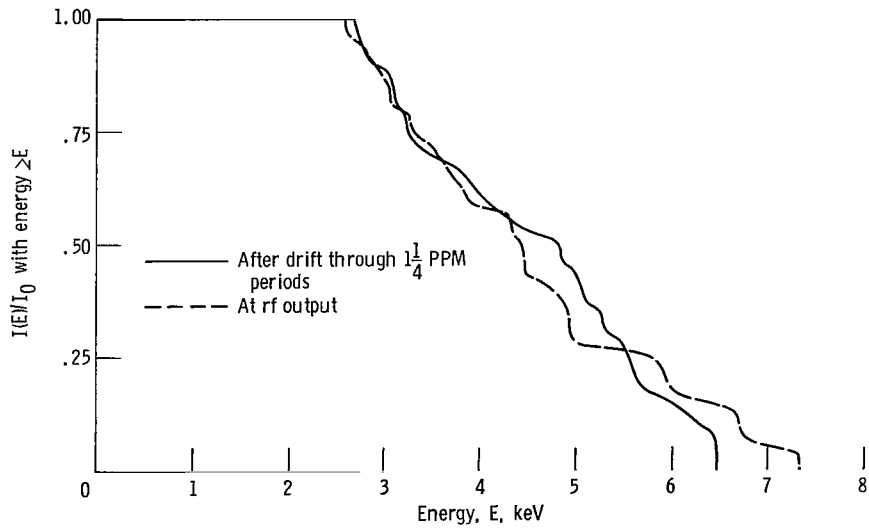


Figure 2. - Spent beam kinetic energy distribution at and past rf output of Watkins-Johnson TWT 3633-5 (disk model).

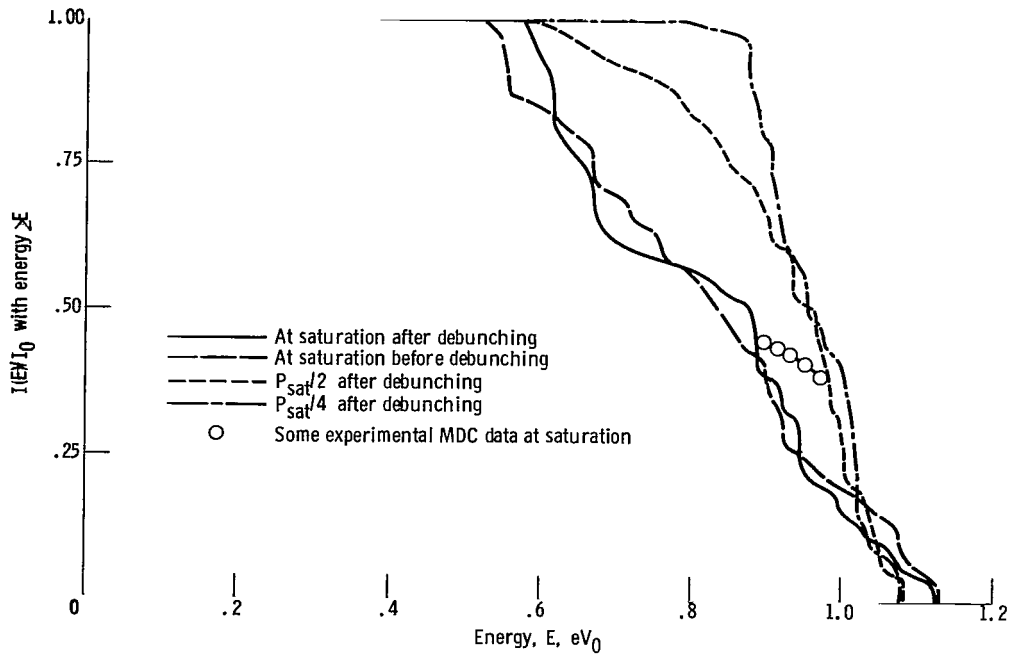


Figure 3. - Analytical spent beam energy distribution of Teledyne MEC TWT 5897C at saturated output power  $P_{sat}$  and at  $P_{sat}/2$  and  $P_{sat}/4$ .

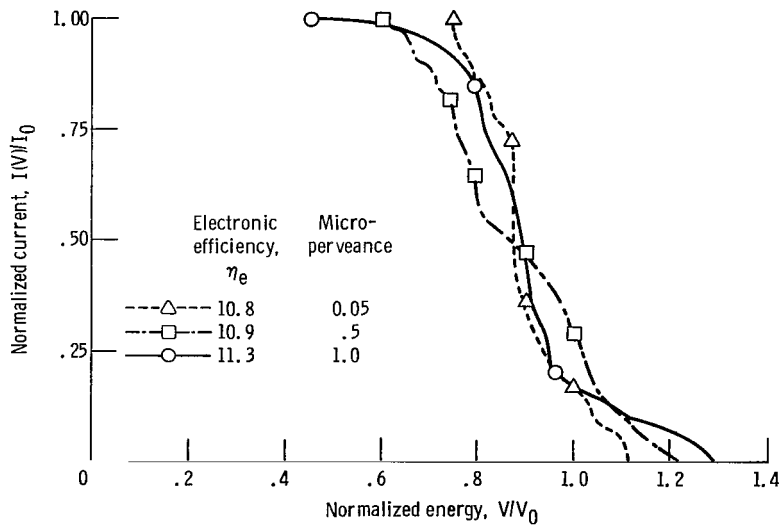


Figure 4. - Computed energy distributions for tubes of same efficiency as function of perveance.

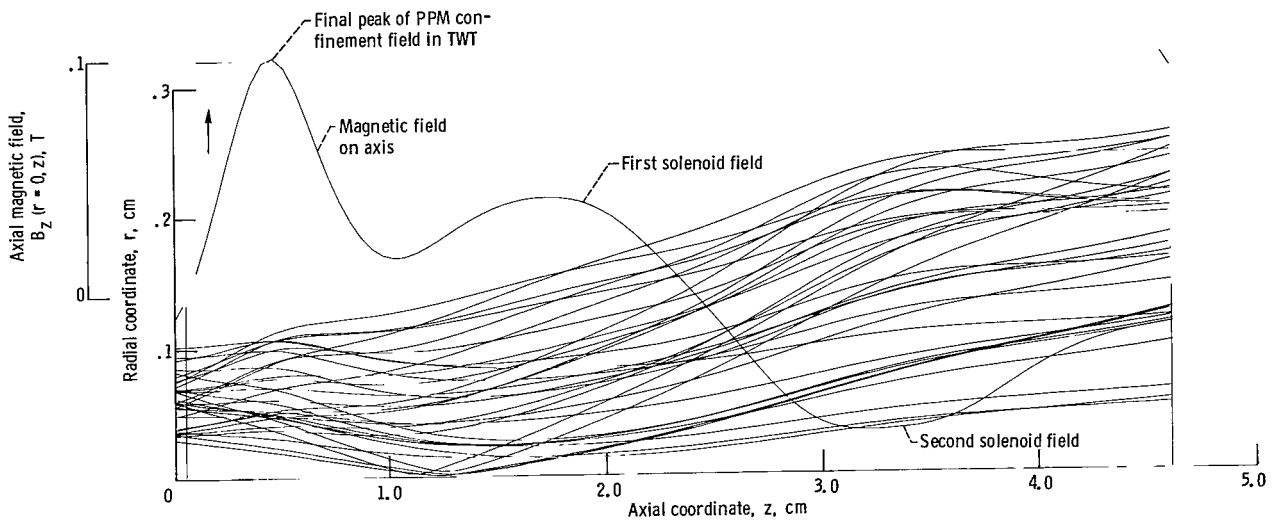


Figure 5. - Typical trajectories in refocusing region and refocusing field profile.



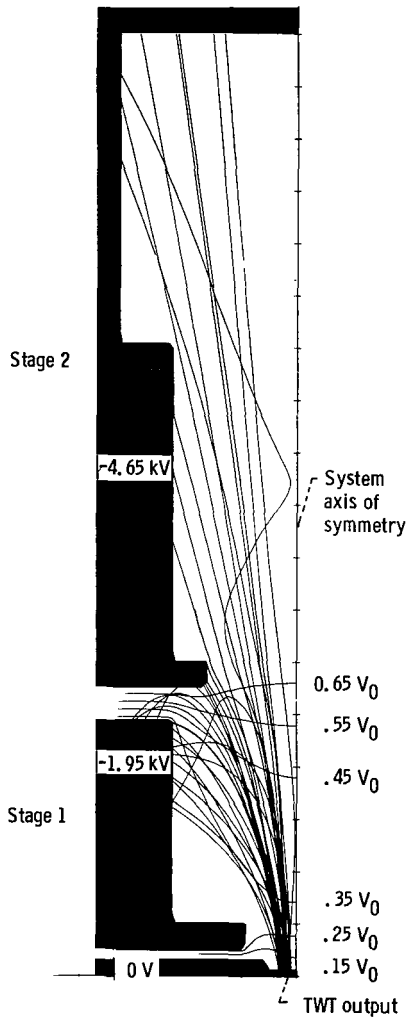


Figure 6. - Electron trajectories in Watkins-Johnson TWT 3633-5 two-stage depressed collector - 32-disk model. Secondary electron emission yield,  $\delta$ , 1.

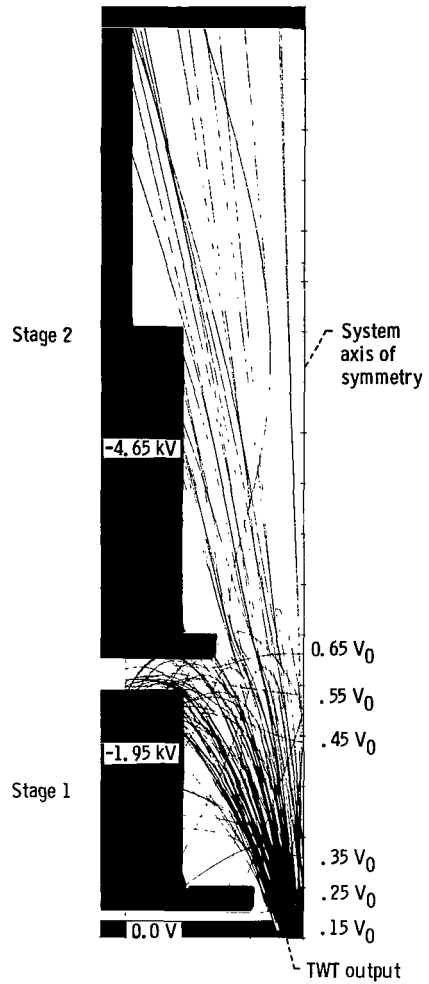


Figure 7. - Electron trajectories in Watkins-Johnson TWT 3633-5 two-stage depressed collector - 96-ring model. Secondary electron emission yield,  $\delta$ , 1.

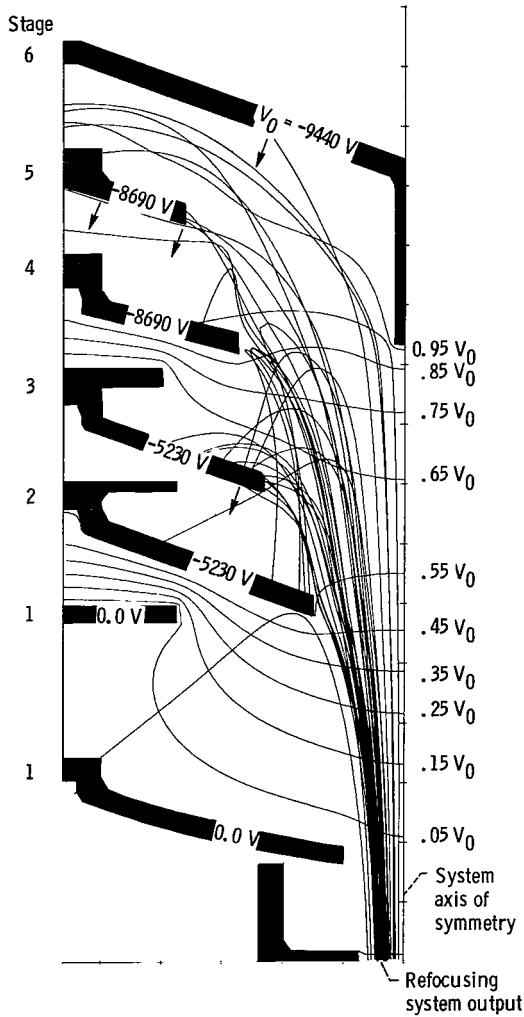


Figure 8. - Electron trajectories in experimental collector with three depressed stages; TWT operating at saturation. Secondary electron emission yield,  $\delta$ , 1/2.

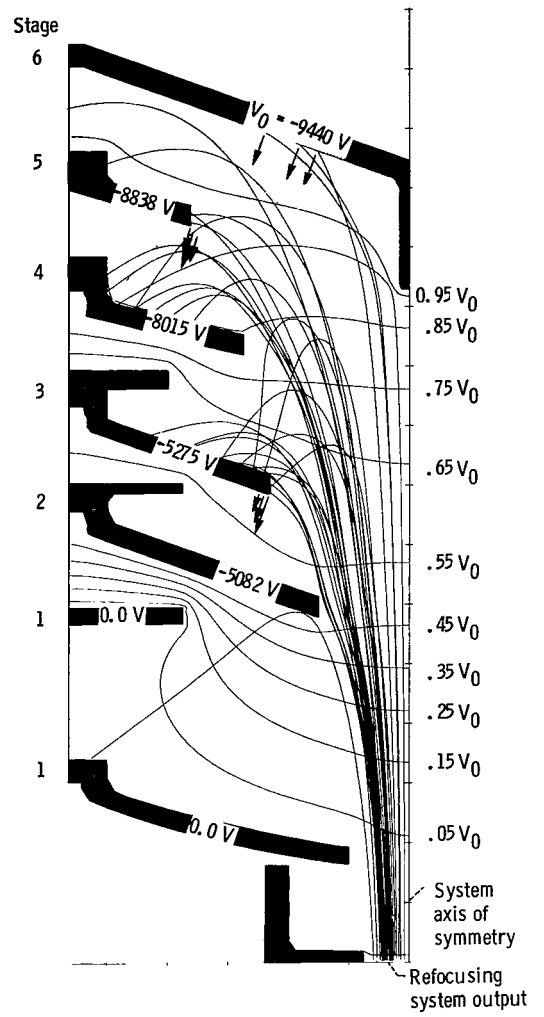


Figure 9. - Electron trajectories in experimental collector with five depressed stages; TWT operating at saturation. Secondary electron emission yield,  $\delta$ , 1/2.

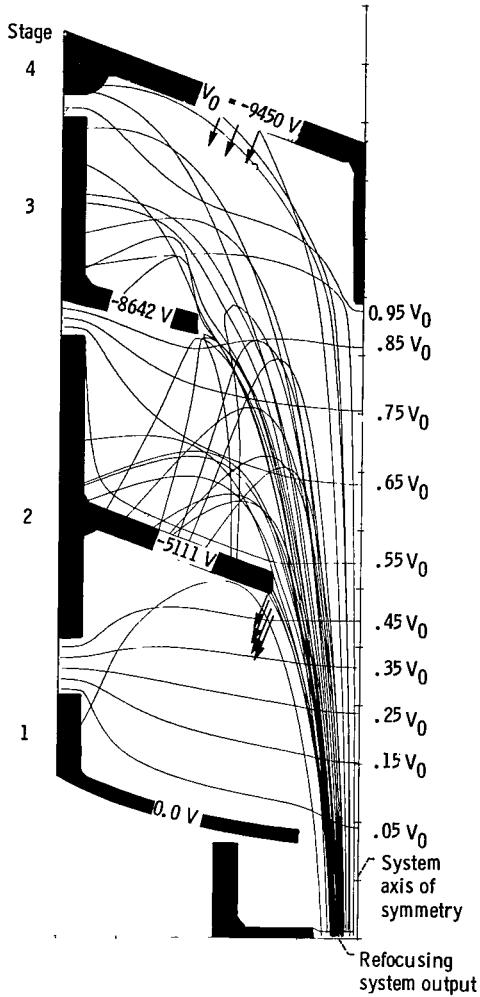


Figure 10. - Electron trajectories in simplified collector with three depressed stages; TWT operating at saturation. Secondary electron emission yield,  $\delta$ , 1/2.

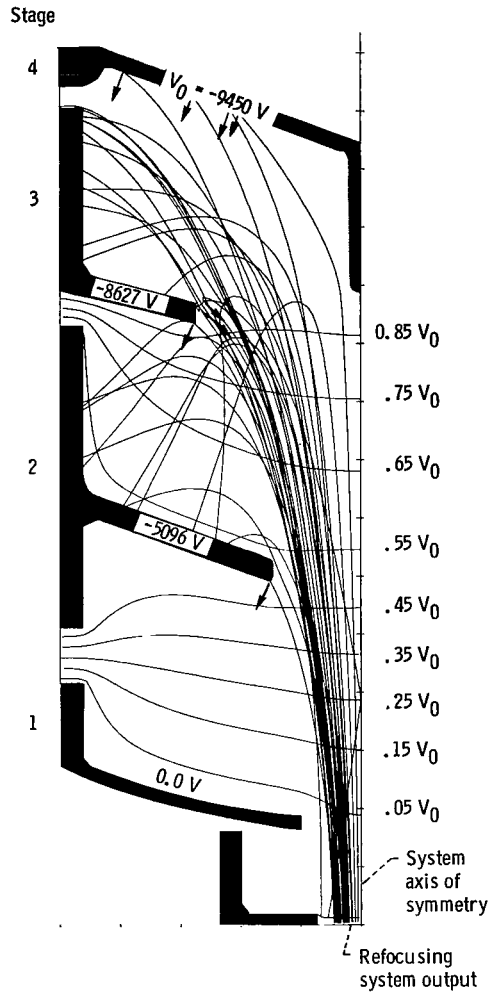


Figure 11. - Electron trajectories in simplified collector with three depressed stages; TWT operating at 3 decibels below saturation. Secondary electron emission yield,  $\delta$ , 1/2.

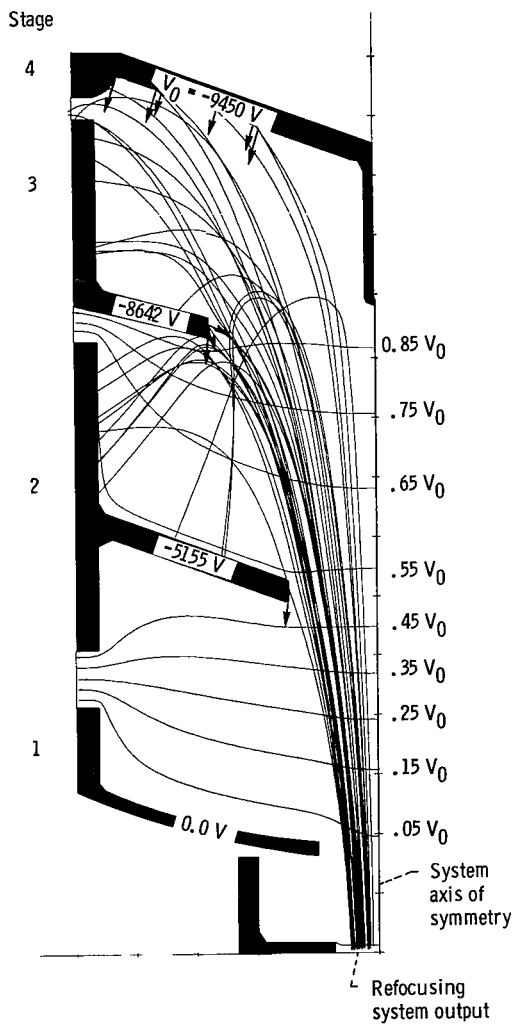


Figure 12. - Electron trajectories in simplified collector with three depressed stages; TWT operating at 6 decibels below saturation. Secondary electron emission yield,  $\delta$ , 1/2.

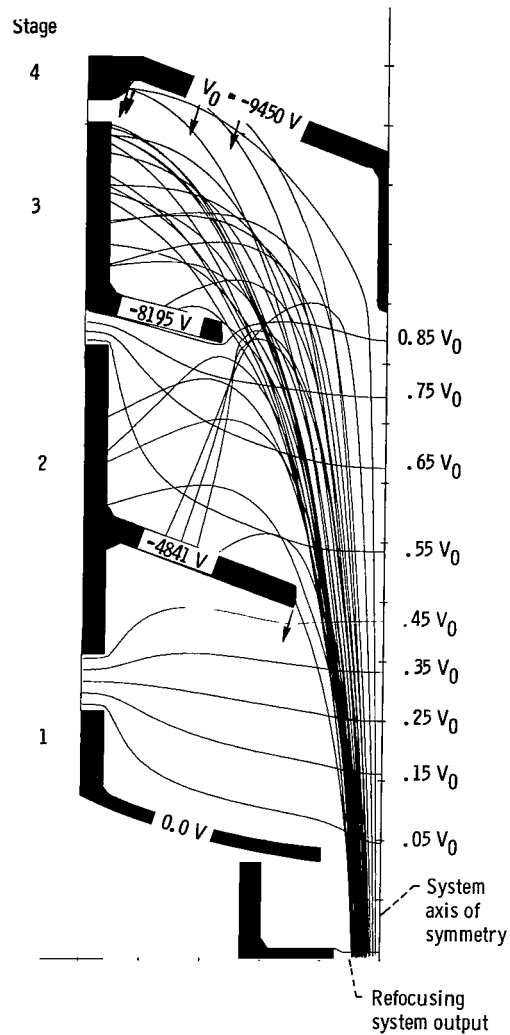


Figure 13. - Electron trajectories in simplified collector with three depressed stages; collector depression reduced 5 percent; TWT operating at 3 decibels below saturation. Secondary electron emission yield,  $\delta$ , 1/2.

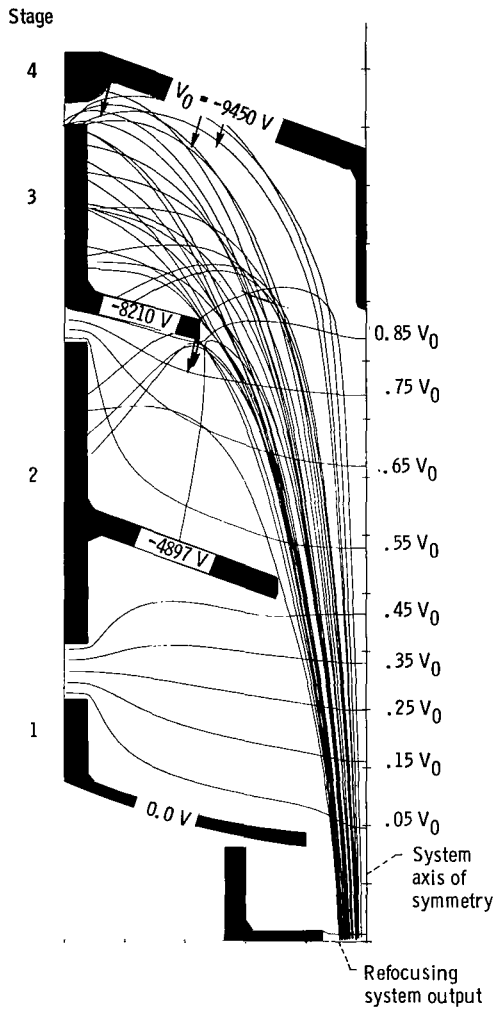


Figure 14. - Electron trajectories in simplified collector with three depressed stages; collector depression reduced 5 percent; TWT operating at 6 decibels below saturation. Secondary electron emission yield,  $\delta$ , 1/2.

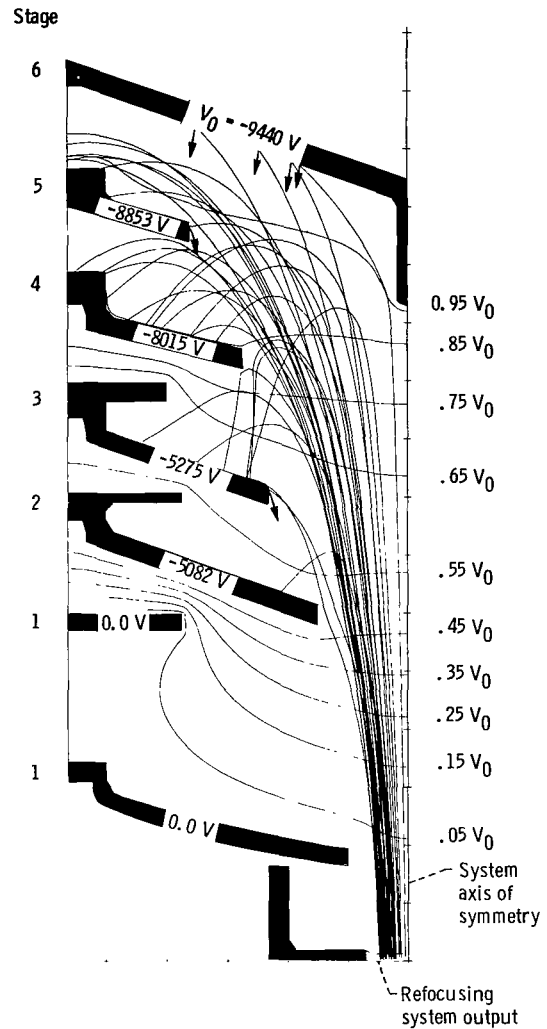


Figure 15. - Electron trajectories in experimental collector with five depressed stages; TWT operating at 3 decibels below saturation. Secondary electron emission yield,  $\delta$ , 1/2.

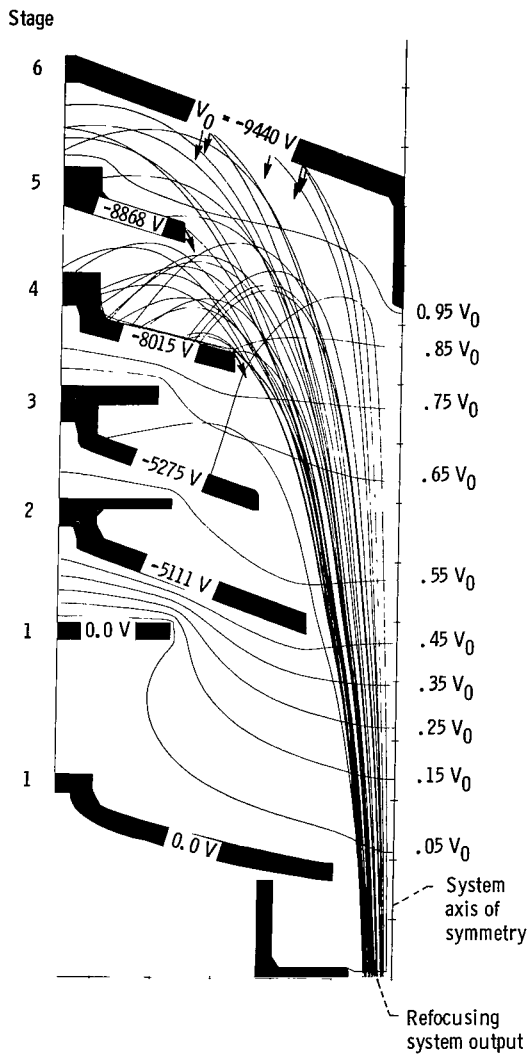


Figure 16. - Electron trajectories in experimental collector with five depressed stages; TWT operating at 6 decibels below saturation. Secondary electron emission yield,  $\delta$ , 1/2.

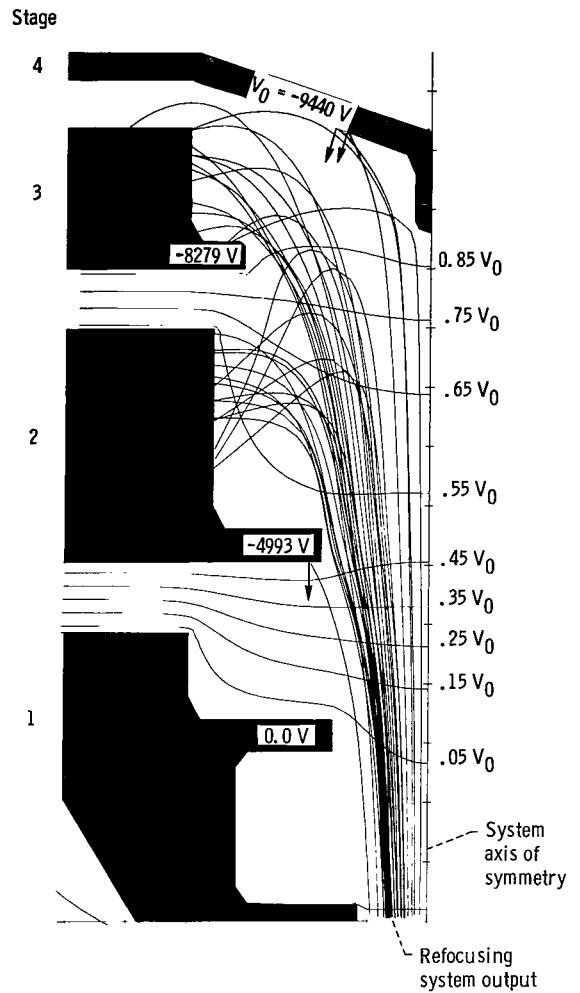


Figure 17. - Electron trajectories in scaled-down collector with three depressed stages; TWT operating at saturation. Secondary electron emission yield,  $\delta$ , 1/2.

1. Report No. <b>NASA TP-1449</b>	2. Government Accession No.	3. Recipient's Catalog No.
4. Title and Subtitle <b>ANALYTICAL PREDICTION WITH MULTIDIMENSIONAL COMPUTER PROGRAMS AND EXPERIMENTAL VERIFICATION OF THE PERFORMANCE, AT A VARIETY OF OPERATING CONDITIONS, OF TWO TRAVELING WAVE TUBES WITH DEPRESSED COLLECTORS</b>		5. Report Date May 1979
7. Author(s) <b>James A. Dayton, Jr.; Henry G. Kosmahl; Peter Ramins; and Norbert Stankiewicz</b>		6. Performing Organization Code
9. Performing Organization Name and Address <b>National Aeronautics and Space Administration Lewis Research Center Cleveland, Ohio 44135</b>		8. Performing Organization Report No. <b>E-9728</b>
12. Sponsoring Agency Name and Address <b>National Aeronautics and Space Administration Washington, D. C. 20546</b>		10. Work Unit No. <b>506-20</b>
15. Supplementary Notes		11. Contract or Grant No.
16. Abstract <p>Experimental and analytical results are compared for two high performance, octave bandwidth TWT's that use depressed collectors (MDC's) to improve the efficiency. The computations were carried out with advanced, multidimensional computer programs that are described here in detail. These programs model the electron beam as a series of either disks or rings of charge and follow their multidimensional trajectories from the rf input of the ideal TWT, through the slow wave structure, through the magnetic refocusing system, to their points of impact in the depressed collector. Traveling wave tube performance, collector efficiency, and collector current distribution were computed and the results compared with measurements for a number of TWT-MDC systems. Power conservation and correct accounting of TWT and collector losses were observed. For the TWT's operating at saturation, very good agreement was obtained between the computed and measured collector efficiencies. For a TWT operating 3 and 6 dB below saturation, excellent agreement between computed and measured collector efficiencies was obtained in some cases but only fair agreement in others. However, deviations can largely be explained by small (&lt;5 percent) differences in the computed and actual spent beam energy distributions. The analytical tools used here appear to be sufficiently refined to design efficient collectors for this class of TWT. However, for maximum efficiency, some experimental optimization (e.g., collector voltages and aperture sizes) will most likely be required.</p>		13. Type of Report and Period Covered <b>Technical Paper</b>
17. Key Words (Suggested by Author(s)) <b>Traveling wave tube Efficiency Multistage depressed collector Electron beam</b>		14. Sponsoring Agency Code
19. Security Classif. (of this report) <b>Unclassified</b>		18. Distribution Statement <b>Unclassified - unlimited STAR Category 33</b>
20. Security Classif. (of this page) <b>Unclassified</b>	21. No. of Pages <b>54</b>	22. Price* <b>A04</b>

\* For sale by the National Technical Information Service, Springfield, Virginia 22161